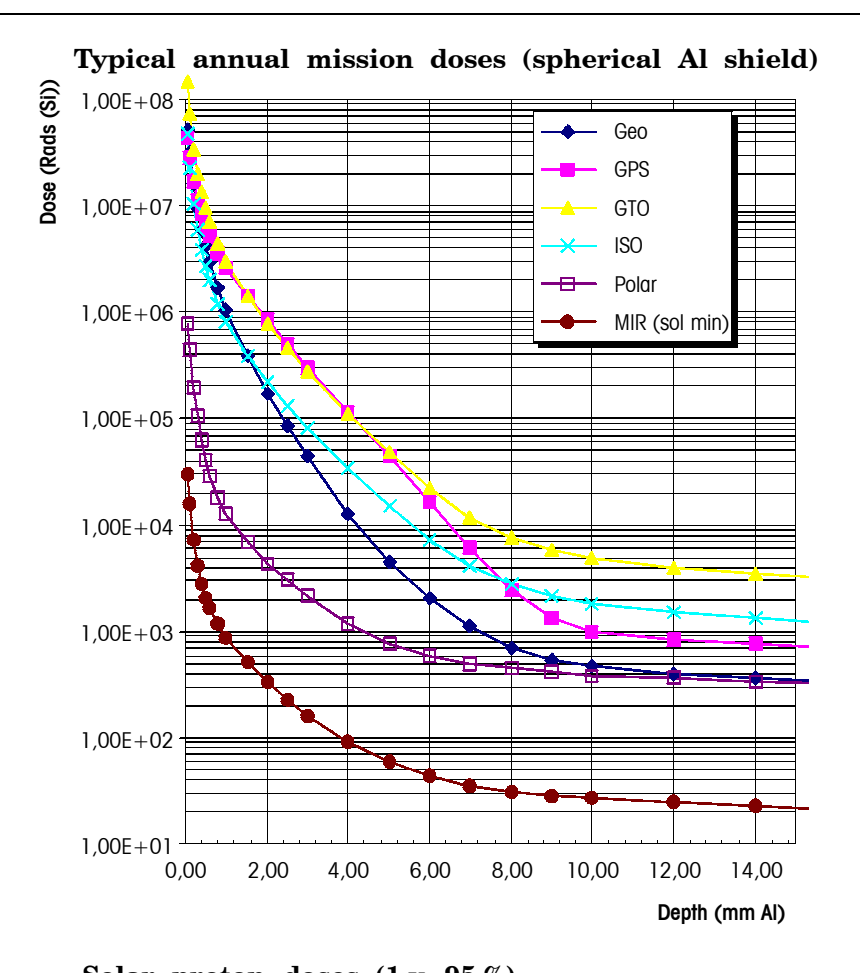


Figure 22: Typical doses predicted for typical missions





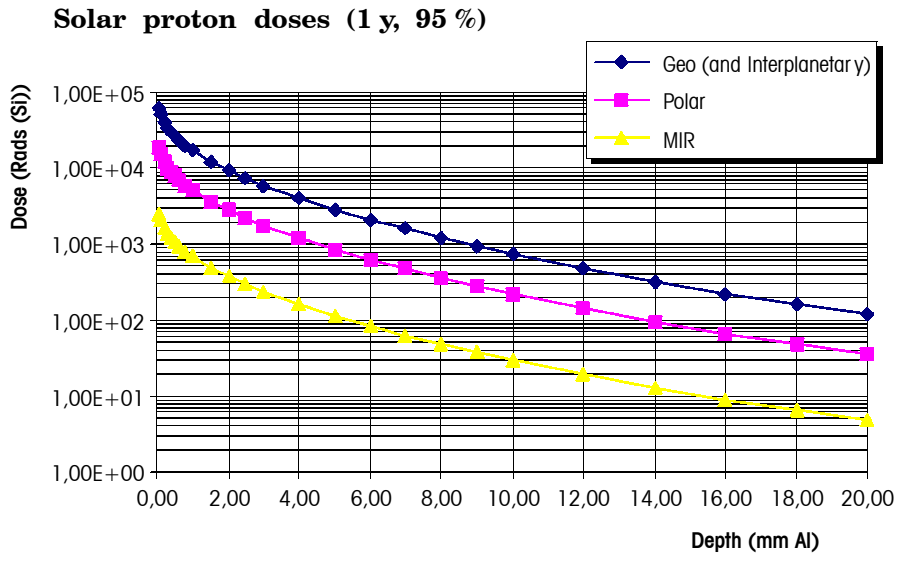


Figure 23: Typical dose-depth curves for Earth-orbits



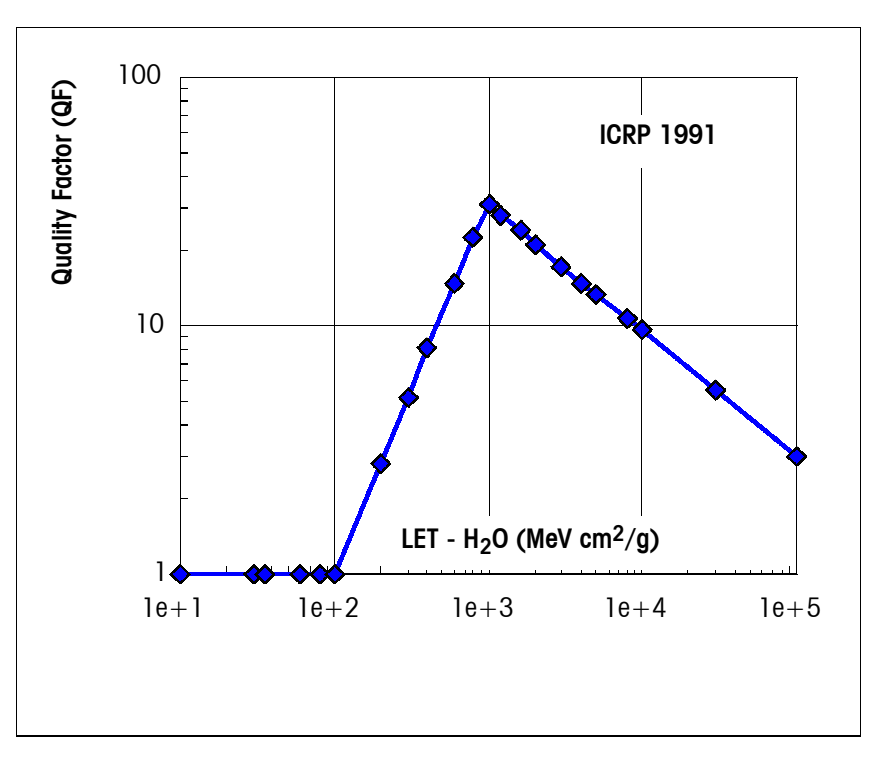


Figure 24: Quality factors for use in dose equivalent calculations for radio-biological effect purposes, as defined by the *ICRP*

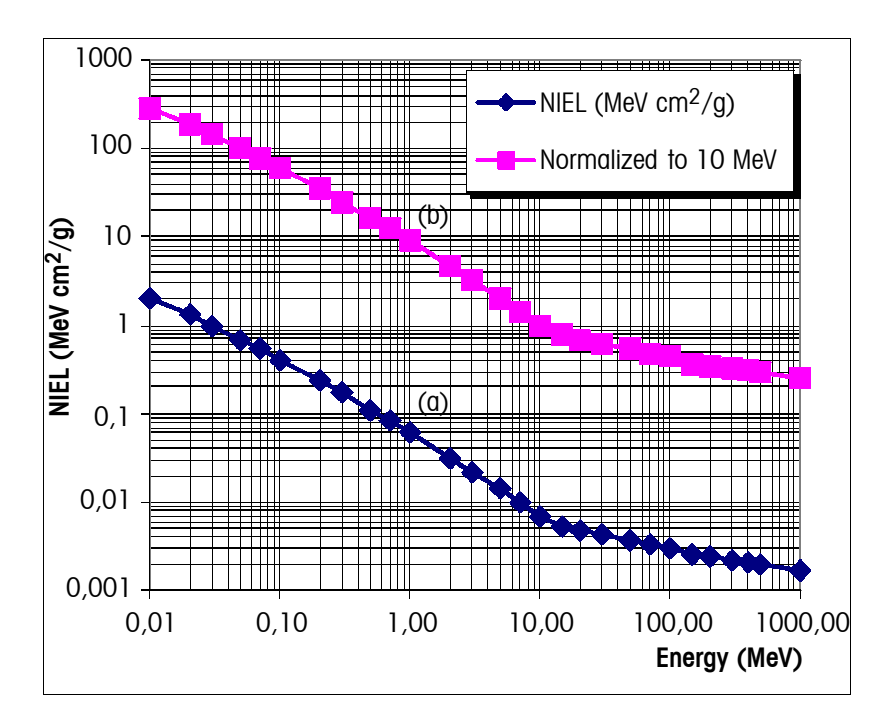


Figure 25: The NIEL curve: (a) energy lost by protons in non-ionizing interactions (bulk, displacement damage); (b) NIEL relative to 10 MeV giving damage-equivalence of other energies



9.8 References

- RD9.1 Hess W.N., "The Radiation Belt and Magnetosphere", Blaisdell Publ. Co..1968.
- RD9.2 Daly, E.J., "The Radiation Belts", Radiation Physics and Chemistry 43, 1, pp.1-18 (in Special Issue on Space Radiation Environment and Effects), 1994.
- RD9.3 NCRP, "Guidance on Radiation Received in Space Activities", Report NCRP-98, National Council on Radiation Protection and Measurements, ISBN 0-929600-04-5, July 1989.
- RD9.4 ECSS, "Human Factors Standard", ECSS-E-TBD.
- RD9.5 ICRP, "1990 Recommendations of the International Commission on Radiological Protection", ICRP Publication 60, Annals of the ICRP 21, 1-3 ISBN: 0-08-041144-4, Pergamon Press, NY and Oxford, 1991.
- RD9.6 Vette J.I., "The AE-8 Trapped Electron Model Environment", NSSDC/WDC-A-R&S Report 91-24, NASA-GSFC, 1991.
- RD9.7 Sawyer D.M. and J.I. Vette, "AP8 Trapped Proton Environment For Solar Maximum and Solar Minimum", NSSDC WDC-A-R&S 76-06, NASA-GSFC, 1976.
- RD9.8 Belian, R.D., T.E. Cayton, R.A. Christensen, J.C. Ingraham,
 M.M. Meier, G.D. Reeves and A.J. Lazarus, "Relativistic electrons in the outer-zone: An 11-year cycle; their relation to the solar wind",
 Proceedings of the Taos Workshop on the Earth's Trapped Particle Environment, Ed, G.D. Reeves, AIP Conference Proceedings 383, 13-18, ISBN 1-56396-540-2, 1986.
- RD9.9 Watts J.W., T.A. Parnell and H.H. Heckman, "Approximate Angular Distribution and Spectra for Geomagnetically Trapped Protons in Low-Earth Orbit", in "High-Energy Radiation Background in Space", AIP Conference Proceedings 186, AIP, NewYork, 1989.
- RD9.10 Kruglanski M. and J. Lemaire, "Trapped Proton Anisotropy at Low Altitude", Technical Note 6, ESA/ESTEC/WMA Contr. 10725, Institut d'Aeronomie Spatiale de Belgique, 1996.
- RD9.11 Bühler P., A. Zehnder, E. Daly and L. Adams, "REM Measurements on-Board MIR in 1995", Cospar General Assembly 1996, to appear in Adv. Sp. Res., 1997–1998.
- RD9.12 Lemaire J., A.D. Johnstone, D. Heynderickx, D.J. Rodgers, S. Szita and V. Pierrard, "Trapped Radiation Environment Model Development (TREND-2)" Final Report of ESA Contr. 9828, Aeronomica Acta 393–1995, Institut d'Aeronomie Spatiale de Belgique/Belgisch Institut voor Ruimte-Aeornomie, ISSN 0065-3713, 1995.
- RD9.13 Brautigam D.H., M.S. Gussenhoven and E.G. Mullen, "Quasi-Static Model of Outer Zone Electrons", IEEE Trans. Nucl. Sci. NS-39,.1797, 1992.
- RD9.14 Singley G.W. and I. Vette J.I., "The AE-4 Model of the Outer Radiation Zone Electron Environment", NSSDC/WDC-A-R&S 72-06, NASA-GSFC, 1972.
- RD9.15 Tranquille C, "Extension to AE-4 Local Time and Statistical Models for Application to AE-8", ESTEC/WMA Internal Memorandum, 1986.
- RD9.16 Feynman J., G. Spitale, J. Wang and S. Gabriel, "Interplanetary Proton Fluence Model: JPL 1991", J. Geophys. Res. 98, A8, 13281-13294, 1993.
- RD9.17 Tranquille C. and E.J. Daly, "An Evaluation of Solar Proton Event Models for ESA Missions", ESA J. 16, 275, 1992.
- RD9.18 King, J.H., "Solar Proton Fluences for 1977–1983 Space Missions", J. Spacecrafts and Rockets, 11, 401, 1974.
- RD9.19 Mathews J. and S. Towheed, OMNIWeb, http://nssdc.gsfc.nasa.gov/omniweb/ mathews@nssdc.gsfc.nasa.gov, Code 633, NASA GSFC, Greenbelt, MD 20771, USA.



- RD9.20 National Geophysical Data Center, "Space Environment Data from NOAA's GOES Satellites", National Geophysical Data Center, Code E/GC2, Dept. 946 325 Broadway Boulder Co 80303 3328 USA., also Space Physics Interactive Data Resource at http://www.ngdc.noaa.gov:8080/.
- RD9.21 Adams, J.H., "Cosmic Ray Effects on MicroElectronics, Part IV", NRL Memorandum Report 5901, Naval Research Laboratory, Washington DC 20375-5000, USA, 1986.
- RD9.22 Tylka, A.J., et al., "CREME96: A Revision of the Cosmic Ray Effects on Micro-Electronics Code", IEEE Trans. Nucl. Sci. NS-44, 2150-2160, 1997.
- RD9.23 Nymmik, R.A., M.I. Panasyuk, T. I. Pervaja, and A.A. Suslov, "A Model of Galactic Cosmic Ray Fluxes", by, Nucl. Tracks & Radiat. Meas, 20, 427–429, 1992.
- RD9.24 Adams J.H., R. Silberberg and C.H. Tsao, "Cosmic Ray Effects on Microelectronics, Part I: The Near-Earth Particle Environment", NRL Memorandum Report 4506, Naval Research Laboratory, Washington DC 20375-5000, USA, 1981.
- RD9.25 Roberts C.S., "Co-ordinates for the Study of Particles Trapped in the Earth's Magnetic Field: A Method of Converting from B,L to R,λ Co-ordinates", J. Geophys. Res. 69, 5089, 1964.
- RD9.26 Stassinopoulos E.G. and J.H. King, "Empirical Solar Proton Model For Orbiting Spacecraft Applications", IEEE Trans. on Aerosp. and Elect. Systems AES-10, 442, 1973.
- RD9.27 Seltzer S., "SHIELDOSE: A Computer Code For Space Shielding Radiation Dose Calulations", NBS Technical Note 1116, National Bureau of Standards, May 1980.
- RD9.28 Petersen E.L., "Approaches to Proton Single-Event-Rate Calculation", IEEE Trans. Nucl. Sci. NS-43, 2 (special issue on Single Event Effects and the Space Environment), 496, 1996.
- RD9.29 Pickel J.C. "Single-Event Effects Rate Prediction", IEEE Trans. Nucl. Sci. NS-43, 2 (special issue on Single Event Effects and the Space Environment), 483, 1996.
- RD9.30 Tada H.Y., J.R. Carter, B.E. Anspaugh and R.G. Downing, "Solar Cell Radiation Handbook", 3rd Edition, JPL Publn. 82–69 (1982); B.E.Anspaughv, "GaAs Solar Cell Radiation Handbook", JPL Publn. 96–9, 1996.
- RD9.31 Hopkinson G.R., C.J. Dale and P.W. Marshall, "Proton Effects in Charge-Coupled Devices", IEEE Trans. Nucl. Sci. NS-43, 2 (special issue on Single Event Effects and the Space Environment), 614, 1996.



10

Particulates

10.1 Introduction

Every spacecraft in Earth orbit is exposed to a certain flux of micrometeoroids and man-made space debris. Collisions with these particles takes place with hypervelocity speed.

Meteoroids are particles of natural origin. Nearly all meteoroids originate from asteroids or comets. The natural meteoroid flux represents, at any instant, a total of about 200 kg of mass within 2000 km of the Earth surface [RD10.1].

Meteoroids that retain the orbit of their parent body can create periods of high flux and are called streams. Random fluxes with no apparent pattern are called sporadic.

Space debris is man-made. Since 1957, more than 3500 launches have led to a current (1996) population of approximately 8000 trackable objects (i.e. larger than about 10 cm in Low Earth Orbits (LEO)) in space. More than 90 % of these objects are space debris, i.e., man made objects that do not serve any useful purpose. About half of the trackable objects are fragments from explosions or from the break up of satellites or rocket bodies. It is expected that there is a much greater number of objects in orbit that cannot be operationally tracked. The number of space debris objects larger than 1 cm is estimated to between 30000 and 130000. Smaller particles are far more abundant still.

The damage caused by collisions with meteoroids and space debris depends on the size, density, speed and direction of the impacting particle and on the shielding of the spacecraft.

Submillimeter sized particles can cause pitting and cratering of outer surfaces and lead to degradation of optical, electrical, thermal, sealing or other properties.

Larger particles can puncture outer surfaces and can cause damage to structure or equipment by penetration and spallation.

Flux models have been developed for both micrometeoroids and space debris. The resulting damage can be assessed through empirically derived design equations which give e.g. penetration capabilities and crater sizes as function of the particle parameters and target properties.

All operational and mitigation aspects related to space debris are not covered within this document. This includes topics like lifetime and re-entry aspects, spacecraft passivation and other debris prevention measures, end-of-life de- or re-orbiting, collision avoidance.



10.2 Analysis techniques

Impact analysis techniques fall naturally into two different categories: larger, trackable pieces and smaller, non-trackable particles.

Objects larger than about 10 cm in LEO and larger than about 1 m in GEO are regularly tracked by Radar.

Trackable orbiting objects, whose orbital elements are known, can be propagated along their orbit and their chance of a future collision with another spacecraft or fragment can be assessed. This deterministic approach provides at the same time all relevant parameters of such a potential collision, like the respective object sizes, impact velocity and direction.

Several data sources of satellites and fragments and some analysis tools for trackable objects have been combined in the European DISCOS tool [RD10.2].

For meteoroids and the abundant smaller space debris particles which cannot be tracked, statistical flux models shall be used.

The meteoroid and debris fluxes are usually specified as a time-averaged flux, F_r , against a single sided, randomly tumbling surface. Flux is defined as number of intercepted objects per unit time and area.

The relevant area for F_r is the actual outer surface area of the spacecraft. One can also define a "cross sectional area flux", F_c , for a randomly tumbling satellite, where the relevant area is the time averaged cross sectional area. For objects with no concave surfaces (no self-shielding): $F_c = 4 F_r$.

For spacecraft which fly with a fixed orientation, the meteoroid and orbital debris fluxes shall be treated as vector quantities and the effects of directionality shall be carefully evaluated. Most impacts from both, meteoroids and space debris occur on forward facing surfaces.

The number of impacts, N, increases linearly with exposed area and with exposure time:

$$N = F \times A \times T$$

where

F is the number of impacts per unit area;

A is the total exposed area;

T is the exposure time.

The numbers of impacts from meteoroids and space debris can be summed to obtain the total number of impacts:

$$N_{tot} = N_{met} + N_{deb}$$

Once N has been determined, the probability of exactly n impacts occurring in the corresponding time interval is given by Poisson statistics:

$$P_n = \left(\frac{N^n}{n!}\right) \times e^{-N}$$

The probability for no impacts, P_0 is thus given by:

$$P_0 = e^{-N}$$

For values of $N \ll 1$ the probability, Q, for at least one impact $(Q = 1 - P_0)$ is equal to N:

$$Q = 1 - e^{-N} \approx 1 - (1 - N) = N$$



10.3 Model presentation

10.3.1 Meteoroids

The isotropic meteoroid flux model given in RD10.3 or the new interplanetary flux model presented in RD10.4 and enhanced in RD10.5 shall be used depending on the analysis requirements and the applicable regimes for each model.

10.3.1.1 Flux model

The isotropic meteoroid model from RD10.3 is described below.

The total average meteoroid flux (sporadic + stream average) can be given in terms of the integral flux $F_{met,0}$ which is the number of particles with mass m or larger per m^2 per year impacting a randomly-oriented flat plate under a viewing angle of 2π . The unshielded interplanetary flux at 1 AU distance from the Sun can be described analytically [RD10.3] as:

$$F_{met,0}(m) = 3,15576 \times 10^{7} (F_1(m) + F_2(m) + F_3(m))$$

where

$$F_1(m) = (2.2 \times 10^3 \, m^{0.306} + 15)^{-4.38};$$

$$F_2(m) = 1.3 \times 10^{-9} (m + 10^{11} m^2 + 10^{27} m^4)^{-0.36};$$

$$F_3(m) = (1,3 \times 10^{-16} \, (m+10^6 \, m^2)^{-0.85};$$
 with m in g.

10.3.1.2 Velocity distribution

Meteoroid velocities near Earth can range from 11 km/s to 72 km/s.

The velocity distribution with respect to Earth to be used with the isotropic reference flux model given in RD10.3 is (number per km/s):

$$g(v) = \begin{cases} 0{,}112 & \text{if } 11{,}1 \le v < 16{,}3 \text{ km/s} \\ 3{,}328 \times 10^5 \text{ } v^{-5{,}34} & \text{if } 16{,}3 \le v < 55{,}0 \text{ km/s} \\ 1{,}695 \times 10^{-4} & \text{if } 55{,}0 \le v < 72{,}2 \text{ km/s} \end{cases}$$

The average velocity of this distribution is close to 17 km/s.

The average impact velocity to an orbiting spacecraft in LEO is 19 km/s.

10.3.1.3 Earth attraction and shielding

The unshielded flux $F_{met,0}$ shall be modified to account for the gravitational attraction (which enhances the meteoroid flux in the Earth proximity) and the geometrical shielding of the Earth (which reduces the flux). The gravitational enhancement factor G_e for the velocity distribution given above is defined as [RD10.1]:

$$G_e = 1 + \frac{R_E}{r}$$

where

 R_E is the mean Earth radius;

r is the orbit radius.

The Earth shielding factor, s_f , for a given surface depends on the spacecraft altitude above the Earth surface and on the relative orientation of the surface normal with respect to the Earth direction.



The average Earth shielding factor is given by:

$$s_f = \frac{(1 + \cos \eta)}{2}$$

with:

$$\sin \eta = \frac{(R_E + 100)}{(R_E + h)}$$

where

 R_E is the Earth radius = 6378 km;

h is the spacecraft altitude in km; 100 km accounts for the atmosphere.

The meteoroid flux to an Earth orbiting spacecraft is then given by:

$$F_{met} = F_{met,0} \times G_e \times s_f$$

10.3.1.4 Mass density

The mass density of meteoroids varies widely from about $0.15~\rm g/cm^3$ to $8~\rm g/cm^3$. According to reference RD10.1 the average density of micrometeoroids larger than $0.01~\rm g$ is assumed to be $0.5~\rm g/cm^3$. Meteoroids smaller than $10^{-6}~\rm g$ are thought to have a higher mean density of $2~\rm g/cm^3$. The recommended value for masses between $10^{-6}~\rm g$ and $0.01~\rm g$ is $1~\rm g/cm^3$. However, there is still a considerable uncertainty about these densities. The reference mass density values to be used for design are given in 10.3.1.9.

10.3.1.5 Directional distribution

The annual average meteoroid flux is usually considered to be omnidirectional with respect to the Earth surface. Relative to an orbiting spacecraft with fixed orientation with respect to the flight direction the meteoroid flux has a directional dependence, introduced by the spacecraft motion, in addition to the Earth shielding effect defined in 10.3.1.3.

The directional dependence of meteoroids shall be calculated numerically by converting the omnidirectional flux to the flux on a spacecraft surface with given surface orientation and spacecraft velocity vector.

10.3.1.6 Meteoroid streams

The meteoroid flux model of sections 10.3.1.1 - 10.3.1.5 gives a yearly average.

Meteoroid streams are accumulations of meteoroids with nearly identical heliocentric orbits. Relative to Earth all particles of a given meteoroid stream have nearly identical impact directions and velocities. Encounters with meteoroid streams typically lasts from a few hours to several days.

At peak activity stream fluxes can exceed the sporadic background fluxes by a factor five or more. Occasionally, very high fluxes (meteoroid storms, the visible meteor background flux can be exceeded by a factor 10000 or more) can be encountered for short periods (1–2 hours). Such a storm is predicted for the Leonid stream in 1998, 1999 or 2000.

Meteoroid streams are believed to consist of relative large particles only (mass > 10^{-8} – 10^{-6} g) with low density (0,5–1,0 g/cm³).

Activity ratios for the major yearly meteoroid streams are given in 10.4.2.2.

Reference meteoroid stream flux models are given in RD10.6 and RD10.7.

10.3.1.7 Interplanetary meteoroid model

A new interplanetary meteoroid flux model was presented in RD10.4 and enhanced in RD10.5. This model is based on five different types of meteoroid populations whose relative contributions depend on the particle size range and the distance from the Sun.



The model includes directional distributions of the populations.

For Earth orbits the meteoroid model predicts similar total fluxes as the reference model in subclause 10.3.1. In addition it includes directional effects.

A drawback for engineering applications is the higher complexity of the model.

10.3.1.8 Regime of applicability

The isotropic meteoroid model given in subclauses 10.3.1.1. - 10.3.1.5. is applicable for all Earth orbits and for interplanetary space at distances around 1 AU from the Sun.

The interplanetary meteoroid model in 10.3.1.7. is applicable for all Earth orbits and for interplanetary orbits.

10.3.1.9 Tailoring guidelines

Values for average mass densities of meteoroids are:

low: 1,0 g/cm³
 nominal: 2,0 g/cm³
 high: 4,0 g/cm³

For analysis of effects the nominal value of 2,0 g/cm³ shall be used.

For the assessment of impact effects the full velocity distribution of meteoroids should be used.

The distribution given in 10.3.1.2. is valid for LEO but can be used for all Earth orbits.

For a preliminary analysis a constant meteoroid impact velocity of 20 km/s shall be used.

A spherical shape shall be assumed to convert particle masses and diameters.

For meteoroid stream fluxes either the model in RD10.6 or in RD10.7 can be used.

For each meteoroid stream the specific particle velocity shall be considered.

For short duration missions (less than about 3 weeks), the contributions of meteoroid streams shall be considered. For longer missions the yearly average model can be used.

10.3.2 Space debris

Due to ongoing updates and extensions of existing space debris environment models no particular standard is defined yet.

As interim solution for space debris, the ESA MASTER-97 [RD10.8] model or the NASA ORDEM-96 model [RD10.9] shall be used, depending on the analysis requirements and depending on the areas of applicability for each model, as defined in annex $\rm H.$

10.3.3 Dust

10.3.3.1 Lunar dust

From Surveyor and Apollo missions, a large amount of information has been gathered about the lunar dust environment.

This information, along with its engineering implications, is summarized in RD10.10.

Approximately 70 % weight of the lunar regolith (i.e. the blanket of rocks and soil, 3 m to 20 m thick that covers the Moon's surface) is composed of particles smaller than 1 mm. 50 % weight of that soil is in turn composed of particles smaller than 50 μ m. This dust is abrasive and sticky due to the high vacuum that allows Van der Waals forces to weld dust grains to surfaces. Therefore dust represents a threat to any functional surface that, once contaminated, cannot be decontaminated.



For details on grain sizes, one should refer to RD10.11.

The models given in RD10.10 and RD10.11 shall be used as reference for Lunar dust.

10.3.3.2 Martian dust

A comprehensive description of the Martian environment can be found in RD10.12. This reference based on the results of the Mariner and Viking missions, contains information about the distribution and optical properties of dust in the atmosphere, the description of e.g. dust storms, as well as a surface model based on information gathered by the Viking Landers. This model includes physical description, chemical properties, physical properties, average bulk density, dielectric constants of surface material.

Recent estimates [RD10.13, RD10.14] place the likelihood of a global dust storm occurring in any one Martian year at about one in three, though with a large variance. In addition, observations made during the Phobos mission in 1989 indicate that the atmosphere can be clearer than the clearest seen by Viking in 1977–78 [RD10.15]. For engineering applications, it is recommended that atmospheric conditions similar to those observed during the Phobos mission are included.

A recent update on wind speed thresholds for dust lifting is given in RD10.16. The threshold friction velocity for 100 μm particles is 1,5 m/s. Higher winds are needed to lift smaller particles, but once lifted much lower winds can maintain them aloft.

The model given in RD10.12 shall be used as reference model for the Martian dust environment, together with the more recent data given in RD10.13 - RD10.15.

It shall be assumed that, in any Martian year, the probability of a global dust storm is 1/3.

10.3.3.3 Cometary dust

The available information on cometary dust is still seen as insufficient to define a general standard model. Two overviews of cometary gas and dust models are given in RD10.17 and RD10.18.

These documents are given for information only. New cometary dust models are presently been developed.

10.4 Reference data

10.4.1 Trackable space debris

The following information on the catalogued space debris population was obtained from the DISCOS [RD10.2] database. The figures show the situation of mid-1996.

The time evolution of the number of trackable objects in orbit is shown in Figure 26.

The altitude dependence for the lower altitudes is given in Figure 27.

The object distribution as function of their inclination is plotted in Figure 28. A concentration at certain inclinations is clearly visible.

10.4.2 Statistical flux models

10.4.2.1 Random plate

Cumulative meteoroid and space debris fluxes (i.e. fluxes of particles of given size or larger) can be obtained directly from the flux models. Table 32 gives the number of impacts /m²/year from one side to a randomly oriented plate for a range of minimum particle sizes. The ORDEM-96 model [RD10.9] was used for the debris fluxes. The results are for an altitude $h=400\,\mathrm{km}$, inclination $i=51,6^\circ$, year 2000, ratio of future to historic debris production rate, N=0,2, and solar activity S=140. The meteoroid fluxes are from the model given in 10.3.1. For meteoroids



a density of ρ = 2,0 g/cm³ and the assumption of spherical shape were used to convert masses to diameters.

Table 33 gives the same results for a polar reference orbit (h = 800 km, $i = 98^{\circ}$, all other parameters are as for Table 32).

Table 34 gives the number of impacts at the geostationary altitude ($h = 36000 \, km$). The space debris fluxes are obtained from the MASTER-97 model [RD10.8]. The model is applicable for sizes of 0,1 mm or larger.

In Figure 29 cumulative meteoroid and space debris fluxes are plotted as function of diameter for h = 400 km and $i = 51,6^{\circ}$ (all fluxes and model parameters are as in Table 32).

Table 32: Cumulative number of impacts, N, from one side to a randomly oriented plate for a range of minimum particle sizes using the ORDEM 96 debris model

N_{deb}	N_{met}	7.7		
		N_{tot}		
$(/m^2/year)$	(/m ² /year)	$(/m^2/year)$		
1,23E+4	1,35E+3	1,37E+4		
3,28E+3	6,38E+2	3,92E+3		
1,53E+3	4,02E+2	1,93E+3		
5,92E+2	2,33E+2	8,25E+2		
3,18E+2	1,68E+2	4,86E+2		
1,64E+2	1,18E+2	2,82E+2		
$4,\!27E+1$	5,15E+1	9,42E+1		
1,81E+1	2,70E+1	4,51E+1		
6,31E+0	9,98E+0	1,63E+1		
3,34E+0	4,58E+0	7,92E+0		
1,64E+0	1,81E+0	3,45E+0		
2,31E-1	2,25E-1	4,56E-1		
5,56E-2	5,79E-2	1,14E-1		
1,02E-2	9,46E-3	1,97E-2		
3,56E-3	2,74E-3	6,30E-3		
1,21E-3	7,12E-4	1,92E-3		
1,53E-4	4,90E-5	2,02E-4		
4,63E-5	9,98E-6	5,63E-5		
1,04E-5	1,32E-6	1,17E-5		
4,07E-6	3,47E-7	4,42E-6		
1,60E-6	8,36E-8	1,68E-6		
3,57E-7	5,22E-9	3,62E-7		
1,90E-7	1,03E-9	1,91E-7		
1,08E-7	1,32E-10	1,08E-7		
6,48E-8	8,17E-12	6,48E-8		
	1,23E+4 3,28E+3 1,53E+3 5,92E+2 3,18E+2 1,64E+2 4,27E+1 1,81E+1 6,31E+0 3,34E+0 1,64E+0 2,31E-1 5,56E-2 1,02E-2 3,56E-3 1,21E-3 1,53E-4 4,63E-5 1,04E-5 4,07E-6 1,60E-6 3,57E-7 1,90E-7 1,08E-7	1,23E+4 1,35E+3 3,28E+3 6,38E+2 1,53E+3 4,02E+2 5,92E+2 2,33E+2 3,18E+2 1,68E+2 1,64E+2 1,18E+2 4,27E+1 5,15E+1 1,81E+1 2,70E+1 6,31E+0 9,98E+0 3,34E+0 4,58E+0 1,64E+0 1,81E+0 2,31E-1 2,25E-1 5,56E-2 5,79E-2 1,02E-2 9,46E-3 3,56E-3 2,74E-3 1,21E-3 7,12E-4 1,53E-4 4,90E-5 4,63E-5 9,98E-6 1,04E-5 1,32E-6 4,07E-6 3,47E-7 1,60E-6 8,36E-8 3,57E-7 5,22E-9 1,90E-7 1,03E-9 1,08E-7 1,32E-10		

The results are for an altitude h=400 km, inclination $i=51,6^{\circ}$, year 2000, ratio of future to historic debris production rate, N=0,2, and solar activity S=140. For meteoroids a density of $\rho=2,0$ g/cm³ and spherical shape were used to convert masses to diameters.



Table 33: Cumulative number of impacts, N, from one side to a randomly oriented plate for a range of minimum particle sizes using the ORDEM 96 model

the Olden 30 model						
Diameter	N_{deb}	$N_{met} \ (/{ m m}^2/{ m year})$	N_{tot}			
(cm)	(cm) $(/m^2/year)$		(/m ² /year)			
0,0001	2,93E+4	1,46E+3	3,08E+4			
0,0002	8,28E+3	6,86E+2	8,97E+3			
0,0003	4,00E+3	4,32E+2	4,43E+3			
0,0005	1,62E+3	2,51E+2	1,87E+3			
0,0007	8,97E+2	1,81E+2	1,08E+3			
0,001	4,81E+2	1,27E+2	6,08E+2			
0,002	1,38E+2	5,54E+1	1,93E+2			
0,003	6,40E+1	2,91E+1	9,31E+1			
0,005	2,46E+1	1,07E+1	3,53E+1			
0,007	1,33E+1	4,93E+0	1,82E+1			
0,01	6,66E+0	1,94E+0	8,60E+0			
0,02	1,25E+0	2,41E-1	1,49E+0			
0,03	4,11E-1	6,23E-2	4,73E-1			
0,05	9,85E-2	1,02E-2	1,09E-1			
0,07	3,78E-2	2,94E-3	4,07E-2			
0,1	1,35E-2	7,66E-4	1,43E-2			
0,2	1,80E-3	5,27E-5	1,85E-3			
0,3	5,56E-4	1,07E-5	5,67E-4			
0,5	1,17E-4	1,42E-6	1,18E-4			
0,7	3,95E-5	3,73E-7	3,99E-5			
1,0	1,86E-5	8,99E-8	1,87E-5			
2,0	2,0 7,02E-6		7,03E-6			
3,0	4,57E-6	1,10E-9	4,57E-6			
5,0	2,92E-6	1,42E-10	2,92E-6			
10,0	1,80E-6	8,79E-12	1,80E-6			
/T)114	C14:4	1- 1 000 1				

The results are for an altitude h=800 km, inclination $i=98^{\circ}$, year 2000, ratio of future to historic debris production rate, N=0.2, and solar activity S=140. For meteoroids a density of $\rho=2.0$ g/cm³ and spherical shape were used to convert masses to diameters.



Table 34: Cumulative number of impacts, N, from 1 side to a randomly oriented plate for a range of minimum particle sizes using the MASTER debris model

Diameter	N_{deb} (*)	N _{met}	N_{tot}		
(cm)	$(/m^2/year)$	(/m²/year)	$(/m^2/year)$		
0,0001		1,23E+3	1,23E+3		
0,0002		5,77E+2	5,77E+2		
0,0003		3,64E+2	3,64E+2		
0,0005		2,11E+2	2,11E+2		
0,0007		1,52E+2	1,52E+2		
0,001		1,07E+2	1,07E+2		
0,002		4,67E+1	4,67E+1		
0,003		2,45E+1	2,45E+1		
0,005		9,04E+0	9,04E+0		
0,007		4,15E+0	4,15E+0		
0,01	2,08E-3	1,64E+0	1,64E+0		
0,02	3,05E-4	2,03E-1	2,03E-1		
0,03	1,14E-4	5,24E-2	5,25E-2		
0,05	2,47E-5	8,57E-3	8,59E-3		
0,07	9,09E-6	2,48E-3	2,49E-3		
0,1	3,23E-6	6,45E-4	6,48E-4		
0,2	3,87E-7	4,44E-5	4,48E-5		
0,3	1,23E-7	9,04E-6	9,16E-6		
0,5	3,09E-8	1,20E-6	1,23E-6		
0,7	1,99E-8	3,14E-7	3,34E-7		
1,0	1,51E-8	7,57E-8	9,08E-8		
2,0	1,10E-8	4,73E-9	1,57E-8		
3,0	1,03E-8	9,30E-10	1,12E-8		
5,0	9,75E-9	1,20E-10	9,87E-9		
10,0	9,35E-9	7,40E-12	9,36E-9		

^(*) The MASTER model is only applicable for sizes of 0,01 cm or larger.

The results are for an altitude h=35786 km, inclination $i=0.5^{\circ}$, and year 2000. For meteoroids a density of r=2.0 g/cm³ and spherical shape were used to convert masses to diameters.

10.4.2.2 Meteoroid streams

The ratio, F, of the cumulative meteoroid stream flux to the average sporadic flux is shown in Figures 30a and 30b for the major yearly streams (taken from RD10.6). Plotted is the activity ratio versus the period of activity based on photographic meteors with mass, m>0.1~g.

When impact fluxes are derived from these activity ratios the different stream velocities (also given in RD10.6) have to be considered.

10.4.2.3 Meteoroids directionality

The present meteoroid flux model assumes an isotropic flux with respect to the Earth surface. For an orbiting spacecraft the Earth shielding and the spacecraft motion both introduce a directional dependence.

The Earth shielding factor is defined in 10.3.1.3.



For a surface with normal pointing towards Earth the flux is reduced by an Earth shielding factor $s_f = \cos^2 \gamma$ relative to a surface pointing exactly away from Earth.

The Earth shielding factor for a surface with normal perpendicular to the Earth direction is given by:

$$s_f = 1 - \frac{1}{\pi}(\eta - 0, 5\sin 2\eta)$$

For other fixed orientations the shielding factor can be obtained by interpolation.

The directionality caused by the spacecraft motion leads to increased fluxes on forward facing surfaces and to reduced fluxes on trailing surfaces.

Combining the two factors the following flux ratios for meteoroids are found for 400 km and 800 km altitudes (using the velocity distribution from 10.3.1.2):

	$400 \mathrm{\ km}$	800 km
Front/random	≈ 2,2	≈ 2,0
Front/rear	≈ 7	≈ 6
Space face/Earth face	≈ 11	≈ 5.4

As resulting effects such as penetration depth or impact plasma generation also depend on parameters such as impact velocity and angle, the directional ratios for these effects can be considerably different from those given above.

10.4.2.4 Debris directionality

For an oriented spacecraft surface the debris fluxes are different for the various surfaces.

The highest space debris fluxes are encountered by forward (ram) facing surfaces. Surfaces on spacecraft in circular Earth orbits which point towards Earth, space or the rear direction can only be impacted by space debris particles in eccentric orbits.

The flux ratio oriented/random surface depends on the particle size and the orbit. For higher inclination orbits impacting fluxes become more peaked towards the flight direction.



10.5 Figures

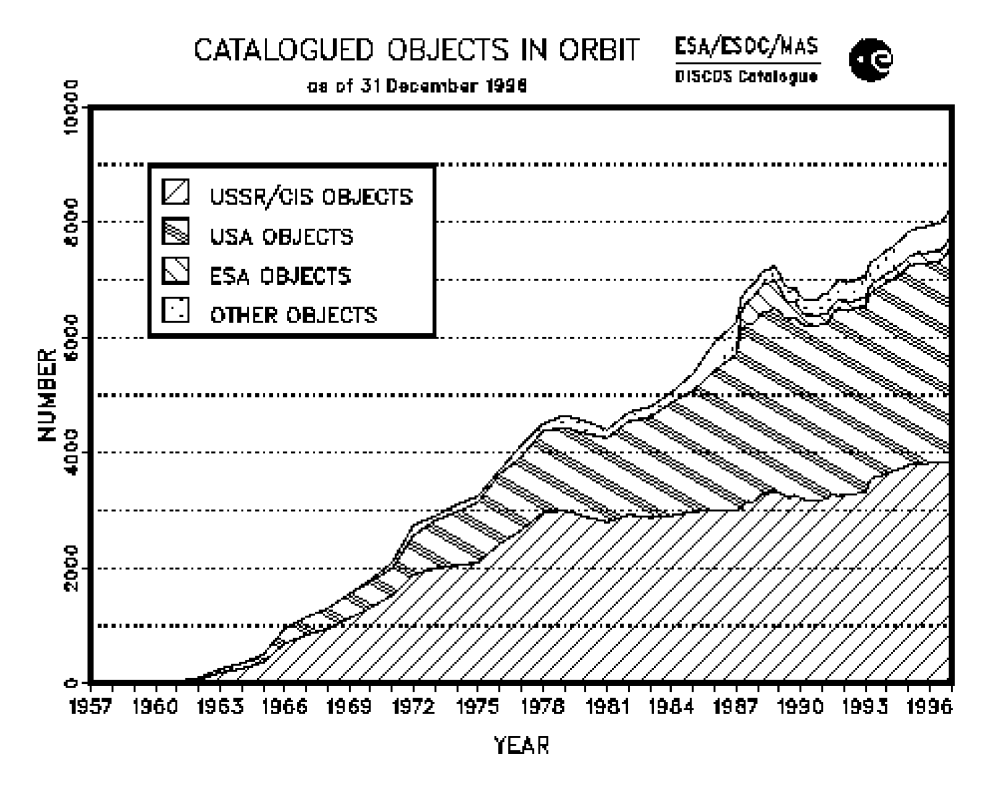


Figure 26: Time evolution of the number of trackable objects in orbit

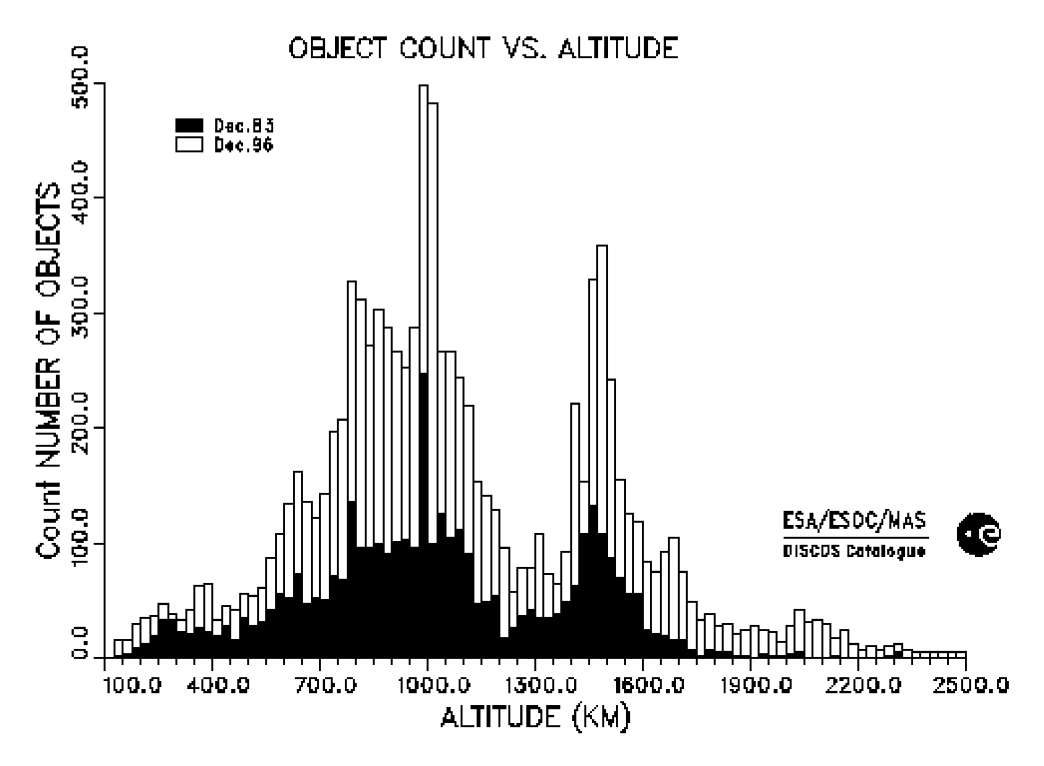


Figure 27: Altitude distribution of trackable objects in LEO orbits



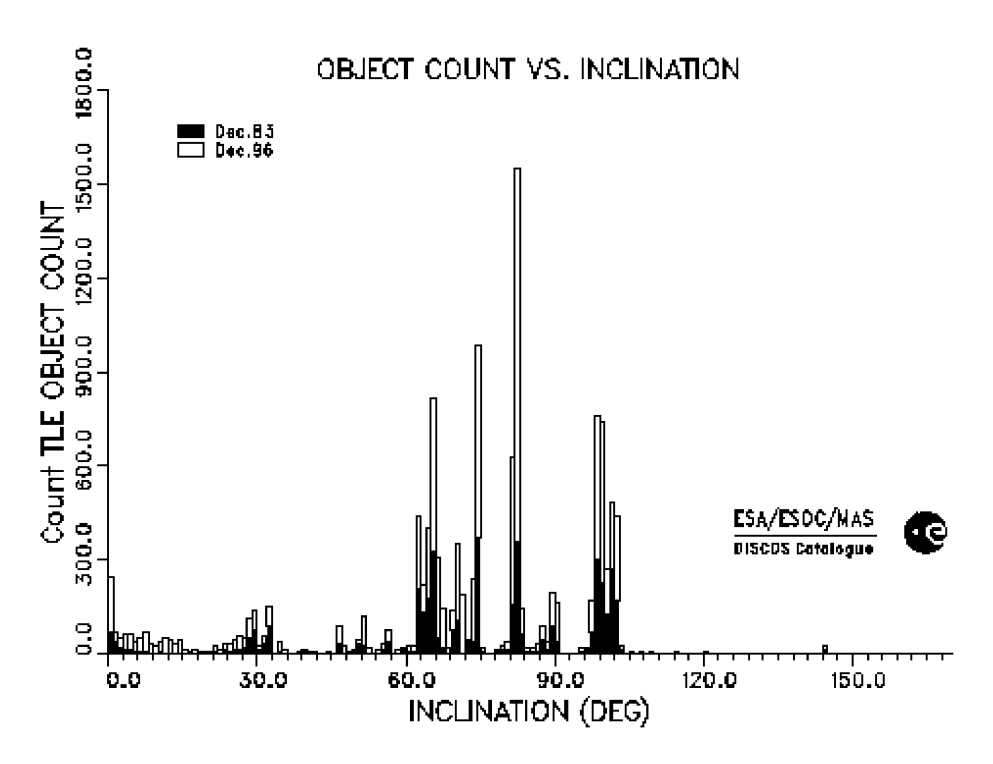
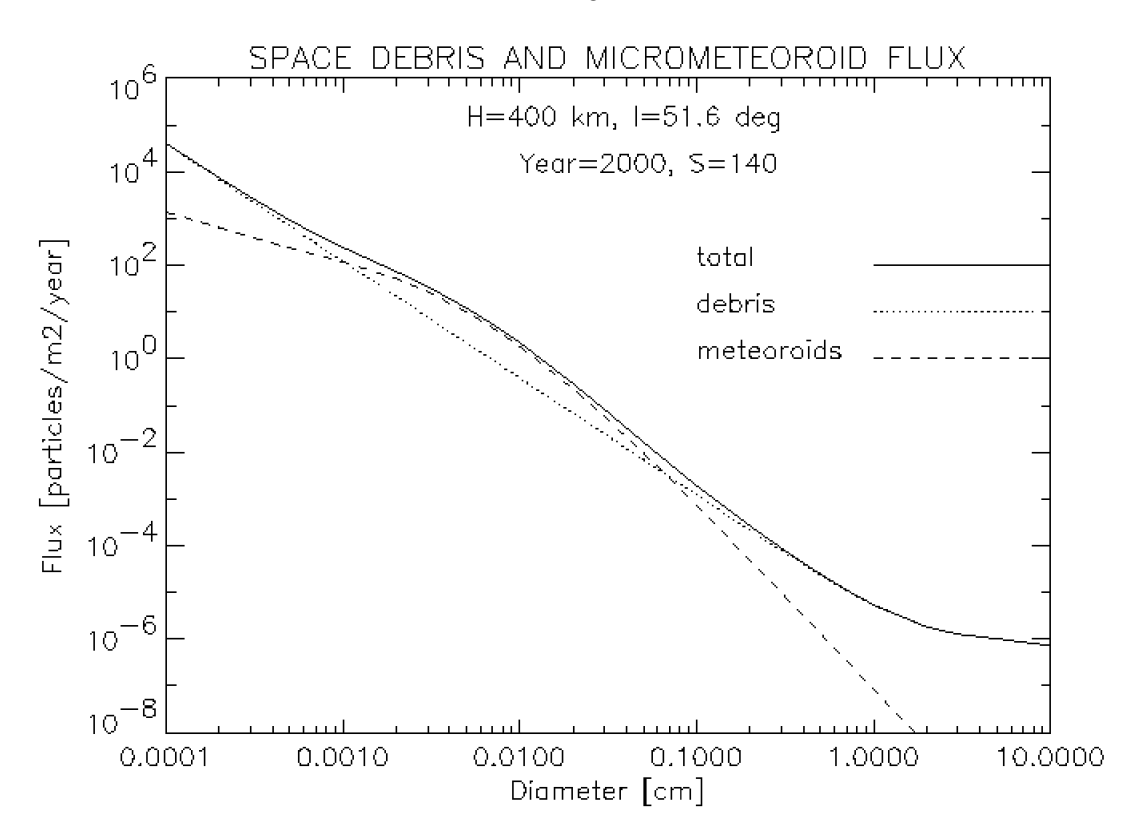


Figure 28: Distribution of trackable objects as function of their inclination



The ORDEM 96 debris model was used. The results are for an altitude h=400 km, inclination $i=51,6^{\circ}$, year 2000, ratio of future to historic debris production rate, N=0,2, and solar activity S=140. For meteoroids a density of r=2,0 g/cm³ and spherical shape were used to convert masses to diameters.

Figure 29: Cumulative number of impacts, N from 1 side to a randomly oriented plate for a range of minimum particle sizes



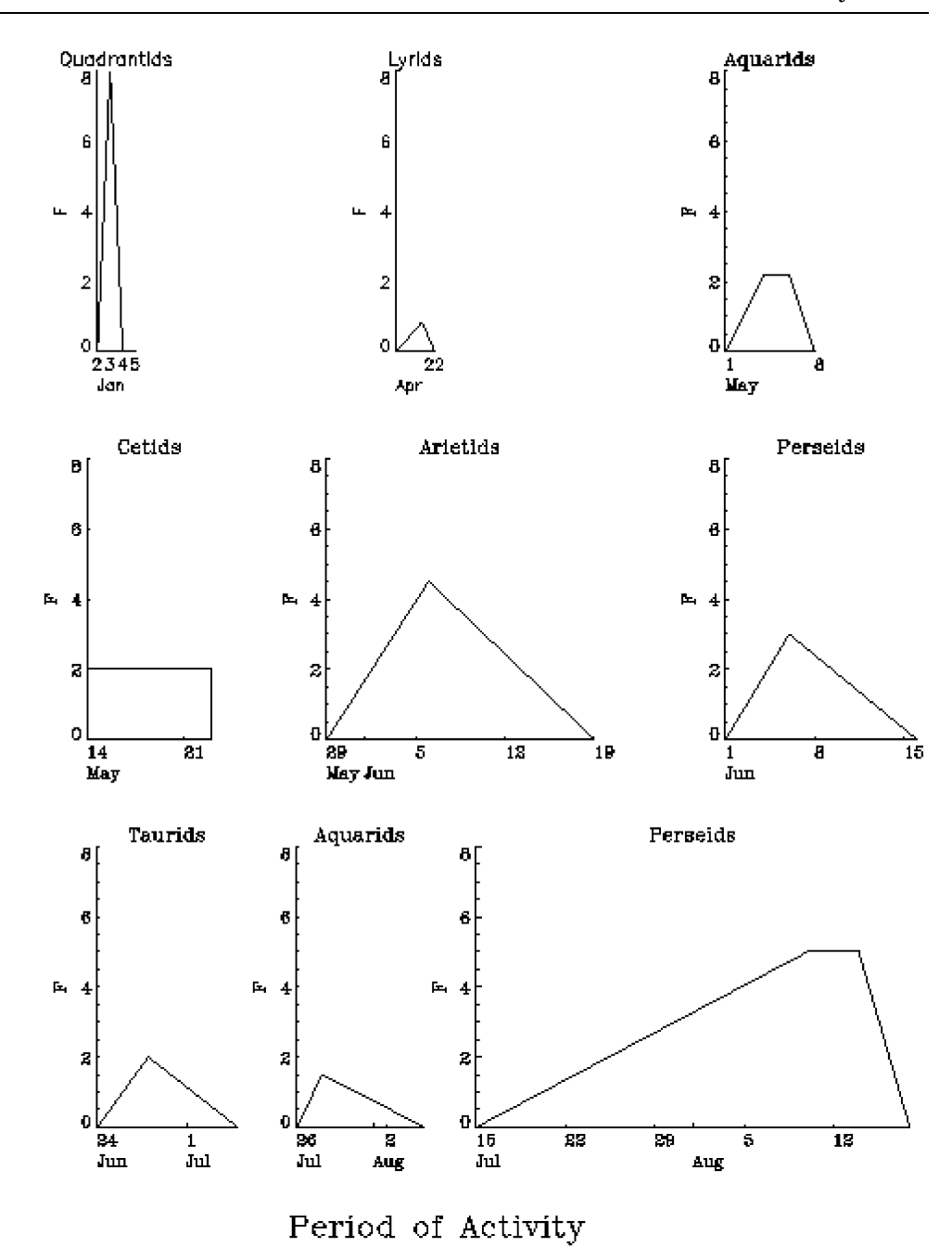
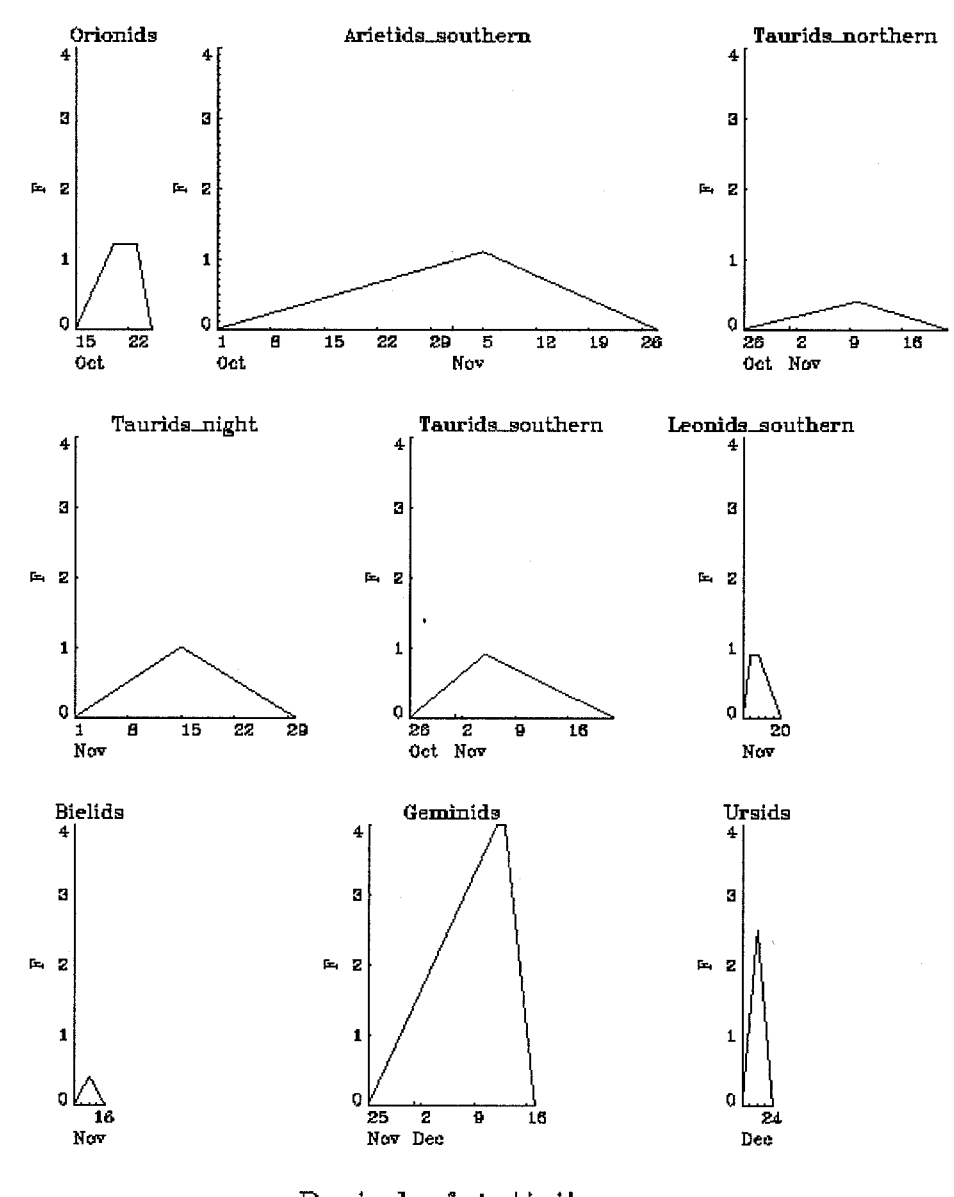


Figure 30: Activity ratio factor versus period of activity for major meteoroid streams

(a) January - August





Period of Activity

 $F = \frac{\text{Cumulative Flux of Stream}}{\text{Average Cumulative Sporadic Flux}}$

Figure 30: Activity ratio factor versus period of activity for major meteoroid streams (continued)

(b) September - December



10.6 References

- RD10.1 "Natural Orbital Environment Guidelines for Use in Aerospace Vehicle Development", B.J. Anderson, Ed. and R.E. Smith, compiler, NASA TM 4527, chapter 7, June 1994.
- RD10.2 Klinkrad H., U. Fuller and J.C. Zarnecki, "Retrieval of Space Debris Information from ESA's DISCOS Catalogue", Proc. ESA Workshop on Space Environment Analysis, Noordwijk, 9-12 October 1990 (ESA WPP-23).
- RD10.3 Grün E., H.A. Zook, H. Fechtig and R.H. Giese, "Collisional Balance of the Meteoritic Complex", Icarus, Vol. 62, p.244, 1985.
- RD10.4 Divine N., "Five Populations of Interplanetary Meteoroids", J. Geophys. Res., Vol. 98, No. E9, 1993.
- RD10.5 Staubach P., E. Grün and R. Jehn, "The meteoroid environment of the Earth", 31th COSPAR Sci. Assembly, Birmingham/UK, July, 1996.
- RD10.6 Cour-Palais B.G., "Meteoroid Environment Model 1969. (Near Earth to Lunar Surface)", NASA SP-8013, 1969.
- RD10.7 Jenniskens P., "Meteor Stream Activity", Astron. Astrophys. Vol. 287, pp 990–1013, 1994.
- RD10.8 Klinkrad H., J. Bendisch, H. Sdunnus, P. Wegener, R. Westerkamp, "An Introduction to the 1997 ESA MASTER Model", Proc. of the Second European Conf. on Space Debris, pp. 217–224, ESA SP–393, May 1997.
- RD10.9 Kessler D.J., J. Zhang, M.J. Matney, P. Eichler, R.C. Reynolds, P.D. Anz-Meador and E.G. Stansbery, "A Computer Based Orbital Debris Environment Model for Spacecraft Design and Observations in Low Earth Orbit", NASA TM 104825, November 1996.
- RD10.10 Katzan C.M., "Lunar dust transport and potential interactions with power system components", NASA CR 4404, 1991.
- RD10.11 Graf J., "Lunar soils grain size catalog", NASA RP 1265, 1993.
- RD10.12 Kaplan D., "Environment of Mars", NASA TM 100470, 1988.
- RD10.13 Martin L.J. and R.W. Zurek, "An analysis of the history of dust activity on Mars", J. Geophys. Res., 98, 3221–3246, 1993.
- RD10.14 Zurek R.W. and L.J. Martin, "Interannual variability of planet-encircling dust storms on Mars", J. Geophys. Res., 98, 3247-3259, 1993.
- RD10.15 Chassefiere E., P. Drossart and O. Korablev, "Post-Phobos model for the altitude and size distribution of dust in the low Martian atmosphere", J. Geophys. Res., 100, 5525–5539, 1995.
- RD10.16 Greeley R., M. Lacchia, B. White, J. Inversen and J.B. Pollack, "Dust on Mars: new values for wind threshold", In XXV Lunar Planet. Sci. Conf., 467-468, 1994.
- RD10.17 Divine N. et al., "The comet Halley dust and gas environment, Space Sci. Rev., Vol. 43, 1-104, 1986.
- RD10.18 Massone L., J. Fertig, E. Grün and G. Schwehm, "A cometary dust environment model for the generation of synthetic images", in "Asteroids, Comets, Meteors II", Conf. Proceedings, Univ. Uppsala, 407-410, 1985.



 $(This\ page\ is\ intentionally\ left\ blank)$



11

Contamination

11.1 Introduction

This clause deals with the induced molecular and particulate environment in the vicinity of and created by the presence of a spacecraft in space. It is meant mainly to aid in the definition of the contamination environment of a satellite. The relevant computer models and tools are presented in annex I.

The quantitative modelling of this contamination environment is very complex. This is due to the high number of materials involved, with a variability of outgassing characteristics. Furthermore, there are interactions of the outgassing products with surfaces, residual gas and with other environmental parameters such as solar radiation and atomic oxygen.

The contamination analysis, which necessarily is very much dependent of a specific project/application, cannot be more detailed in this standard. ECSS-Q-70-01 [RD11.3] defines amongst others the requirements to be followed and guidelines to be taken into account in order to control the particulate and molecular contamination within the specified limits during mission.

The user shall:

- estimate the sensitivity of his system or equipment with regard to contamination;
- identify the contamination sources on-board;
- evaluate with all appropriate means the expected contamination levels or quantities present in critical areas, taking into account the mechanisms of transport and fixation of contaminants.



11.2 Molecular contamination

11.2.1 Sources of molecular contamination

11.2.1.1 Primary sources

11.2.1.1.1 Outgassing of organic materials

Outgassing of organic materials can be approached as a surface evaporation combined with a diffusion for bulk contaminant species. These species can be either initially present components, or decomposition products.

Initially present outgassing species can be:

- water;
- solvents;
- additives:
- uncured monomeric material;
- lubricants;
- ground contamination species, due to e.g. processes, test, storage, handling, pre-launch and launch.

The decomposition products are due to exposure of molecular materials to other environments, such as:

- thermal:
- solar radiation, electromagnetic and charged particles;
- atomic oxygen;
- impacts by micrometeoroids or debris;
- electrical discharges and arcing.

These products consist of lower molecular weight (higher volatility) species than the original species.

11.2.1.1.2 Plumes

Plume species can result from combustion, unburned propellant vapours, incomplete combustion products, sputtered material and other degradation products from a propulsion or attitude control system and its surroundings swept along with the jet.

Plumes can also be produced by dumps of gaseous and liquid waste materials of the environment control and life support systems in manned spacecraft or by leaks in systems or internal payloads. Overboard disposal of materials cause increased molecular column densities and can cause molecular deposition. Plumes can consist of gaseous (molecular) species, liquid droplets and solid particles. Particles can also be formed due to icing or presence of inorganic material during water dumps.

Return flux or back flow is possible due to ambient scattering, self scattering or diffusion processes.

11.2.1.1.3 Pyrotechnics and release mechanisms

During operation of pyrotechnics or other release mechanisms gases can evolve.

11.2.1.2 Secondary sources

A surface can act as a secondary source if an incoming contaminant molecule reflects (not accommodate, stick or condense on the surface) or if it has a limited residence time on that surface. Secondary sources can for example be solar panels having a higher temperature than the surrounding surfaces.



11.2.2 Transport mechanisms

11.2.2.1 Reflection on surface

A molecule reflects on a surface when the accommodation coefficient during a collision is zero, i.e. when there is no energy transfer between the molecule and the surface during that collision. A reflection of a molecule is always specular, although this is dependent on surface roughness, r.m.s.

11.2.2.2 Re-evaporation from surface

A molecule having a non-zero residence time can re-evaporate from a surface. Re-evaporation is diffuse, i.e. the molecule is leaving the surface following a Lambertian distribution law.

11.2.2.3 Migration on surface

A molecule accommodated on a surface can migrate over that surface.

11.2.2.4 Collision with residual (natural) atmosphere

The contamination environment shall take into account the collision between the contamination species and the residual atmosphere. This interaction results in an ambient scattering of the contamination species, and can sometimes lead to an increase in the local pressure.

11.2.2.5 Collision with other outgassed molecules

The contamination environment shall take into account the collision between two contamination molecules. This interaction results in self-scattering of the contamination species.

11.2.2.6 Ionization by other environmental parameters

A molecule can be ionized due to interaction with (V)UV or charged particles (electrons, protons, ions) and subsequently be attracted by a charged surface.

11.3 Particulate contamination

11.3.1 Sources of particulate contamination

11.3.1.1 Sources inherent to materials

- Particles originating from manufacturing (machining, sawing), handling (e.g. for brittle materials such as certain paints) or wear (friction).
- Degradation of binder under different environments (e.g. AO, UV) resulting in loose filler.
- Crack formation and subsequent flaking as a result of thermal cycling.
- Formation of particles due to oxidation in an atomic oxygen environment.

11.3.1.2 Sources external to materials

- Dust particles can be caused by atmospheric fall-out (dust) during assembly, integration and storage or by human sources during such activities (e.g. hair, skin flakes, lints or fibres from garments).
- Particles can be produced during spacecraft propulsion or attitude control operations, the functioning of moving parts (such as shutters), and water dumps.
- Particles can result from micrometeoroid or debris impacts on materials.



11.3.2 Transport mechanisms

11.3.2.1 (Acoustic) vibrations

Vibrations due to launch, (attitude control) manoeuvring and docking. Pyrotechnic shocks can cause particles to migrate from one surface to another.

11.3.2.2 Electrostatic attraction

Particles can be charged due to their interaction with ambient plasma, or photo emission and subsequently attracted by electrically-charged surfaces.

11.3.2.3 Other mechanisms

For specific missions other mechanisms can have an effect on the particles, such as:

- drag, due to the residual atmosphere in the lowest Earth orbits;
- radiation pressure due to solar radiation;
- gravitational tide, e.g. re-attraction to spacecraft.

11.4 Effect of contamination

The primary concerns of contamination are related to the degradation of space-craft system or sub-system performances due to the presence of:

- Deposited species onto a critical surface:
 - (thermo-)optical properties, such as transmission, reflection, absorption, scattering;
 - tribological properties, outgassing of lubricant, friction due to particles;
 - electrical properties, such as surface conductivity, secondary emission and photo-emission.
- Glow or other surface/gas reactions.
- Free flying species in the field of view of sensors:
 - light scattering (star trackers);
 - light absorption;
 - background increase (natural environment analysis).

The effect of a contamination can be altered by the exposure to other environmental parameters, e.g. UV can increase the absorption due to photo-degradation (darkening) of the deposited contaminant, atomic oxygen can have a cleaning-up effect on hydrocarbon material, but can also form non-volatile SiOx that can further trap other contaminants.

11.5 Models

11.5.1 General

 $(Worst\ case)\ outgassing\ modelling\ can\ be\ based\ on\ VCM-test\ results,\ differentiating\ between\ CVCM\ (low\ vapour\ pressure,\ condensable\ material)\ and\ TML\ (sum\ of\ condensable\ and\ non-condensable\ material).$

More sophisticated outgassing/condensation models takes into account the data of outgassing or mass flow rates, surface accommodation and sticking coefficients as obtained by e.g. the VBQC-test [RD11.4] or the ASTM E1559 test [RD11.5].



11.5.2 **Sources**

11.5.2.1 Outgassing

For a material that outgasses at a constant rate, independently of the quantity present, such as e.g. during evaporation or sublimation from a bulk, the process can be described as a zero order reaction.

$$\frac{dm}{dt} = k$$

where

 $\frac{dm}{dt}$ is the outgassing rate (g cm⁻² s⁻¹);

k is the reaction constant.

The weight-loss through evaporation, at a temperature T is given by RD11.6

$$\frac{dm}{dt} = 0,04375 \times P_s \times \left(\frac{M}{T}\right)^{1/2}$$

where

 P_s is the vapour pressure in hPa;

 $\frac{dm}{dt}$ is the weight loss per unit area in g cm⁻² s⁻¹;

M is the molecular mass;

T is the temperature in K.

The outgassing is often described as a first order reaction [RD11.7], i.e. the material outgasses at a rate that is proportional to the mass available, and using Arrhenius law temperature dependency. Important parameters for the outgassing rate are temperature, exposed surface area (or the surface available for evaporation), surface morphology, dimensions of the material (characteristic dimension, thickness).

$$\frac{dm}{dt} = -km$$

The factor k can be seen as a measure for the temperature dependent time constant (τ) of the outgassing phenomenon.

$$k = \frac{1}{\tau}$$

Integration of

$$\frac{dm}{dt} = \frac{m}{\tau}$$

gives

$$m = m_0 \exp(-t/\tau)$$

Assuming the Arrhenius relation to be valid

$$\tau = \tau_0 \exp(-E/RT)$$

it is possible to determine the outgassing as function of temperature.

The mass loss can be expressed as

$$m_{loss} = m_0 - m = m_0 (1 - \exp(-t/\tau))$$



11.5.2.2 Plumes

Evaluation of plumes of thrusters or vents is often described by specific application related models. Parametric descriptions of plumes constitute an interesting alternative to spacecraft designers.

The mass flux Φ of a plume can be expressed in the most generic form

$$\Phi(r,\Theta) = f\left(r,\Theta,\frac{dm}{dt}\right)$$

where

 $\Phi(r, \Theta)$ is the flux at a given position from the vent;

r is the radial distance from the vent;

 Θ is the angle from the centerline of the vent;

dm/dt is the mass flow from the vent;

where, moreover, the function *f* depends on the plume type. However this formula can in general be reduced in a good approximation to the product

$$\Phi(r,\Theta) = A\left(\frac{dm}{dt}\right) f_1(\Theta) r^{-2}$$

where

A is a normalization coefficient.

For a thruster, the function f_I is peaked around $\Theta = 0$ and can be expressed as a sum of decreasing exponentials [RD11.8] or as a (high) power law of $\cos(\Theta)$ or both [RD11.9]. It is in some extent specific of each thruster.

Plumes from vents are more standard and the f_1 function can consequently be fixed: the mass flux is approximated by the following engineering model:

$$\Phi(r,\Theta) = \left\lceil \frac{(n+1)}{(2\pi)} \right\rceil \left(\frac{dm}{dt} \right) \cos^n(\Theta) r^{-2}$$

where $1 \le n \le 2$ is used for space station design. The divergence is larger than the one of thrusters.

11.5.3 Transport of molecular contaminants

11.5.3.1 Transport between surfaces

11.5.3.1.1 General

The following subclauses only deal with the methods and models for transport of neutral molecules (11.2.2.4 and 11.2.2.5). There is no available model of ion transport devoted to contamination (11.2.2.6).

Three levels of complexity and accuracy in modelling the transport of neutral molecular contaminants can be distinguished.

11.5.3.1.2 Simplest view factors

This model simulates collisionless transport. In such a case the fraction of contaminants coming from surface i to surface i is given by the view factor V_{ij} of surface i seen from surface j (including the cosine factor coming from the Lambertian emission law). These view factors are similar to the ones of radiative thermal analysis. They can be computed geometrically or by Monte-Carlo ray tracing. The incident mass on a surface i is then given by

$$S_j V_{ij} \frac{dm_j}{dt}$$

where j runs over all surfaces and dm_j/dt denotes the outgassing mass rate of surface j.



11.5.3.1.3 Simplified Monte-Carlo

Collisions of contaminants are simulated in a simplified way, the density and speed of possible partners for molecular collisions are given a priori:

- for ambient scatter, the ambient density and speed are easily known, but wakes (or "shades") are usually not treated;
- for self-scatter, the contaminant density is very simplified and usually taken proportional to $1/r^2$ and with spherical symmetry.

This simplifying assumption has a consequence: the fraction of contaminants coming onto surface i from surface j is still a constant (depending on assumed densities) that can be called an effective view factor. It results from the view factor (11.5.3.1.2) for collisionless processes diminished by the fraction of scattered molecules and increased by molecules outgassed in other directions but redirected to surface j due to collisions. The deposition rate is then computed similarly to the case in 11.5.3.1.2.

This method is usually limited to one collision per molecule because the uncertainties due to the densities given a priori increase with collision number. This effective view factors can conveniently be computed by Monte-Carlo ray-tracing method.

Both methods 11.5.3.1.2 and 11.5.3.1.3 can include other contaminant sources such as vents and plumes. The view factors are then replaced by interception factors.

11.5.3.1.4 True Monte-Carlo (Direct Simulation Monte-Carlo, DSMC)

This computes multiple collisions in a realistic way. The collision probabilities are computed auto-coherently from the densities given by the simulation. This method is more time consuming and requires more work for programming (in particular, contrarily to 11.5.3.1.2 and 11.5.3.1.3., it requires a meshing of volume and not only of spacecraft surfaces).

Either method can be better suited, depending on the spacecraft configuration. A potential contamination of a sensitive protected surface through multiple collisions shall require a precise DSMC simulation. In simpler cases, when contamination essentially happens in line-of-sight, it shall be more appropriate to use the less time-consuming and more widespread methods of 11.5.3.1.2 and 11.5.3.1.3.

11.5.3.2 Surface transport

Reflections on surfaces (11.2.2.1) and re-evaporation (11.2.2.2) are easy to implement and are usually included in models, the latter (re-evaporation) often as part of the outgassing process. Migrations on surfaces on the contrary are complex processes and there is no commercial available model.

11.5.3.3 Transport of particles

As mentioned in 11.3.2 particulate transport is governed by several phenomena:

- a. atmospheric drag
- b. solar radiation pressure
- c. differential gravitational effects (with respect to spacecraft) which result in tide effects
- d. particulate charging and subsequent electrostatic effects

among which the first three may be computed by methods similar to spacecraft orbit computing, whereas point d. requires specific modelling to access particulate charging in a plasma and potential map around spacecraft. The dominant phenomena are most commonly modelled: point a. atmospheric drag, first, and also point d. that gets important in GEO. Points b. and c. can become dominant in cases when points a. and d. become small (high altitude and no charging).



A last aspect of particulate transport is their interaction with walls. Sticking and accommodation coefficients are, however, very difficult to assess.

Most particulate contamination models remain in the field of research. Very few of them seem to be transferable to other users (only code described here in informative annex I.10: OPT).

11.6 References

- RD11.1 ECSS-Q-70-04, Space product assurance: A thermal vacuum test for the screening of space materials (former ESA PSS-01-702).
- RD11.2 ASTM E-595, Method for Total Mass Loss and Collected Volatile Condensable Materials from outgassing in a vacuum environment.
- RD11.3 ECSS-Q-70-01, Space product assurance: Contamination and cleanliness control (former ESA PSS-01-201).
- RD11.4 Van Eesbeek M. and A. Zwaal, "Outgassing and contamination model based on residence time", ESA SP232, Proc. of the 3rd European Symp. on spacecraft materials in a space environment, Noordwijk, The Netherlands, 1-4 Oct 1985.
- RD11.5 ASTM E-1559, Method for contamination outgassing characteristics of space materials.
- RD11.6 Dushman S., "Scientific Foundations of Vacuum Technique", Wiley & Sons, Inc, New York-London.
- RD11.7 Scialdone J., "Characterisation of the outgassing of spacecraft materials", SPIE Vol. 287 Shuttle Optical Environment, 1981.
- RD11.8 Trinks H., "Exhaust Plume Databook Update Version No. 3 / ESA/ ESTEC Contract 7590/87/NL/TP".
- RD11.9 Simons G.A., "Effect of Nozzle Boundary Layers on Rocket Exhaust Plumes", AIAA Journal, Tech. Notes, vol. 10, No. 11, pp. 1534–1535, 1972.



Annex A (informative)

It is the purpose of these informative annexes to provide supplementary information to the main text. All these annexes are called up in the main text. There is a one-to-one correspondence between the sections in the body of the document. Therefore, the main body section number is mentioned in each informative annex section title.

In several areas of natural and induced environments, models and tools are undergoing rapid evolution and development. Therefore, where appropriate, likely or possible future models are indicated. It is expected that in future revisions of this Standard, models which are outlined in the informative annexes become the standards referenced in the main body.



 $(This\ page\ is\ intentionally\ left\ blank)$



Annex B (informative)

Gravitation

B.1 Related tools

The GRIM4 series of European global Earth gravity field modes has been developed through cooperation between GeoForschungs-Zentrum Potsdam (GFZ, Germany) and Groupe de Geodesie Spatiale (GRGS, France). The GRIM4 model exists as a satellite only version GRIM4-S and a combined solution GRIM4-C. The GRIM4-S series of satellites is derived from optical, laser and Doppler tracking and is complete up to degree and order 50. Combination with gravity anomaly and altimetry data provides the GRIM4-C solution with coefficients complete up to degree and order 60.

The United States Department of Defense Mapping Agency (DMA) has produced the World Geodetic System (WGS) Earth gravitation models, the most recent of which WGS-84 provides harmonic coefficients to degree and order 180. The model is based on Doppler tracking data of near-Earth satellites, laser-ranging data on LAGEOS and STARLETTE, satellite altimetry data over the oceans and mean gravity anomalies derived from surface observations.

The new EGM96 model, developed jointly by NASA Goddard Space Flight Center (GSFC), the National Imagery and Mapping Agency (NIMA, formerly DMA) and The Ohio State University, provides a more accurate reference surface for the topography, improves models of the ocean circulation, improves orbit determination for low-orbiting satellites, and contributes to global and regional studies in tectonics and geodynamics. The new spherical harmonic model, is complete to degree 360, corresponding to a global resolution of about 55 km. EGM96 incorporates newly released surface gravity data from around the globe, over three decades of precise satellite tracking data and altimeter measurements of the ocean surface from the TOPEX/POSEIDON, ERS-1 and GEOSAT satellites.

B.2 Effects

A number of simple analytic expressions [RDB.1] exist which provide approximate engineering solutions for perturbations to a satellite orbit about the Earth.

The Earth is appreciably oblate, the equatorial diameter being 42,77 km greater than the polar diameter. Changes in the gravity field caused by this oblateness lead to the major perturbations to a satellite orbit. First, the orbital plane of the satellite rotates about the Earth axis in a direction opposite to the satellite motion; and secondly, the major axis of the orbit rotates in the orbital plane. A number of simple analytic expressions exist which assume that the Earth is sym-



metric about its polar axis and also consider only the dominant terms in the harmonic expansions.

The rate of nodal regression is given to first order by:

$$\dot{\Omega} = -\frac{3nC_{20}R_{\rm E}^2\cos i}{2a^2(1-e^2)}$$

The rate of precession of the line of apsides is given to first order by:

$$\dot{\omega} = \frac{3nC_{20}R_E^2(4 - 5\sin^2 i)}{4a^2(1 - e^2)}$$

where

a is the semimajor axis of the satellite orbit;

e is the eccentricity of the orbit;

i is the inclination of the satellite orbit;

 Ω is the right ascension of ascending node of the orbit;

 ω is the argument of perigee of the orbit;

$$n \qquad \qquad \sqrt{\frac{GM_{\oplus}}{a^3}}$$

 C_{20} is the spherical harmonic coefficient representing the flattening of the Earth.

These perturbations to the satellite trajectory are exploited by mission designers to achieve preferred orbital configurations optimized to a particular application.

A Sun-synchronous orbit (one where the orbital plane remains nominally fixed relative to the Sun) can be achieved by matching the nodal regression rate Ω to the average rotation rate of the Earth around the Sun. Thus by setting Ω to 0,9856 °/day and substituting in the appropriate values of a, e, R_E , and C_{20} , we see that Sun-synchronisity is only possible for retrograde ($i > 90^\circ$) orbits.

The precession of the line of apsides ω is zero when the orbital inclination is set to 63,4°. This characteristic is exploited in the so-called Molniya orbit which employs a highly eccentric orbit and a frozen perigee is the southern hemisphere to provide communication coverage to high northern latitudes.

A geosynchronous orbit (one where the period of the orbit of a satellite matches the daily rotation of the Earth on its axis) can be achieved by matching the period of the orbit T to 1436 min by varying the semimajor axis of the orbit ($a_{geos} = 42\,164,5$ km) where:

$$T=\frac{2\pi}{n}$$

The longitudinal variation of the Earth gravitational field has a significant influence on geostationary orbits. The terms representing the ellipticity of the Earth's equatorial section (C_{22} and S_{22}) and oblateness (C_{20}) combine to provide the so-called triaxiality perturbation resulting in a longitudinal drift from the stable points (105,3° W and 75,1° E) of the Earth's potential field which represents an East-West station-keeping problem for a geostationary satellite.

Flury [RDB.2] provides an expression for the longitudinal acceleration:

$$\ddot{\Lambda} = k^2 \sin 2(\Lambda - \Lambda_0)$$

 $\Lambda-\Lambda_0$ is the departure from the stable point and where

$$k^2 = -18\sqrt{C_{22}^2 + S_{22}^2}\omega_\oplus \frac{a_\oplus^2}{a_s^2} = 1,7 \times 10^{-3} \, {
m o/day}^2$$

 ω_{\oplus} is the sidereal rotation rate of the Earth;



 a_{\oplus} is the mean equatorial radius of the Earth;

 $a_{\rm s}$ is the semimajor axis of the synchronous orbit.

For satellites at low altitude (<1 000 km), the orbital perturbation due to aerodynamic forces can be significant. The passage of a satellite through an atmosphere can induce drag and lift forces. The drag force acts in the opposite direction to the satellite velocity vector relative to the atmosphere, the lift force acting perpendicular to this velocity vector. Lift forces can normally be neglected for most satellites except when precise orbit determination is required. The drag force has the dominant influence on the satellite trajectory and acts to reduce the semimajor axis and eccentricity of the orbit, and thus in turn the orbital lifetime. King-Hele has developed simple analytic expressions relating the change in a satellite orbit to the aerodynamic forces acting on it. For a circular orbit the orbital lifetime is given by:

$$L = \frac{Hm}{\sqrt{GM_{\oplus} \, a \rho SC_D}}$$

where

H is the density scale height of the atmosphere (see clause 7);

 ρ is the atmospheric density at distance from Earth a (see clause 8);

S is the profile area of the satellite;

 C_D is the drag coefficient of the satellite (see clause 7).

The gravitational attraction of the Moon and Sun influences the orbit of a satellite about the Earth. The major influence is a cyclic variation in the inclination and eccentricity of the orbit. This manifests in geosynchronous orbit as a periodic variation in the orbital inclination requiring North-South station keeping to maintain a nominally geostationary orbit. Cook [RDB.3] has derived expressions for the average rates of change of orbital elements due to the gravitational attraction of a third body.

Solar radiation pressure can also perturb a satellite trajectory from the nominal Keplerian orbit. The major influence of solar radiation pressure (see clause 6) is an increase in orbital eccentricity. At geosynchronous altitudes this can be significant and leading to active stationkeeping while at lower altitudes the effect can be neglected.

The relative magnitudes of the accelerations due to each of the perturbing sources are compared in Table B-1.

B.3 Gravitational field at the surface of a planet

The gravitational accelerations F/m at the surface of the planets given below are derived from their respective masses M and equatorial radii R.



Table B-1: Planetary gravitational characteristics

Planet	Equatorial radius, R (km)	Mass, M (kg)	<i>GM</i> (km ³ s ⁻²)	F/m (ms ⁻²)
Mercury	2420	$3,345 \times 10^{23}$	22322	3,5
Venus	6200	$4,881 \times 10^{24}$	325657	8,5
Earth	6378	$5,974 \times 10^{24}$	398600	9,8
Mars	3400	$6,452 \times 10^{23}$	43049	3,7
Jupiter	71370	$1,900 \times 10^{27}$	126754940	25,9
Saturn	60400	$5,687 \times 10^{26}$	37946762	11,1
Uranus	23530	$8,722 \times 10^{25}$	5819566	10,5
Neptune	22300	$1,033 \times 10^{26}$	6895788	13,8

B.4 Uncertainties

The 1σ errors associated with the spherical harmonic coefficients for JGM-2 given in Table 2 for \overline{C}_{nm} and Table 3 for \overline{S}_{nm} are given below in Table B-2 and Table B-3, respectively. The errors should be interpreted with caution as many of the coefficients have highly correlated errors, especially for higher degree terms and the zonal coefficients.

Table B-2: Covariance errors in normalized coefficients \overline{C}_{nm} (units of 10^{-6}) from JGM-2 model to degree (n) and order (m) 9

					n				
		${f 2}$	3	4	5	6	7	8	9
	0	0,0001090	0,0000261	0,0002600	0,0001570	0,0003540	0,0003620	0,0005210	0,0005730
	1		0,0004170	0,0002350	0,0008440	0,0004870	0,0012000	0,0009020	0,0013500
	2	0,0001240	0,0002660	0,0004270	0,0006760	0,0008020	0,0012400	0,0011400	0,0016000
	3		0,0002010	0,0002290	0,0003910	0,0006450	0,0008340	0,0011500	0,0013200
m	4			0,0002100	0,0002510	0,0003700	0,0005470	0,0007900	0,0010100
	5				0,0002490	0,0001980	0,0003580	0,0004520	0,0007230
	6					0,0002440	0,0001630	0,0003520	0,0004600
	7						0,0003130	0,0002032	0,0003780
	8							0,0003820	0,0002840
	9								0,0004780

Table B-3: Covariance errors in normalized coefficients \overline{S}_{nm} (units of 10^{-6}) from JGM-2 model to degree (n) and order (m) 9

					n				
		2	3	4	5	6	7	8	9
	1		0,0004160	0,0002280	0,0008490	0,0004880	0,0011800	0,0008910	0,0012700
	2	0,0001240	0,0002920	0,0004390	0,0007060	0,0008380	0,0012700	0,0012100	0,0015900
	3		0,0001970	0,0002210	0,0003840	0,0006160	0,0008390	0,0010900	0,0013300
m	4			0,0002120	0,0002450	0,0003710	0,0005310	0,0007880	0,0009880
	5				0,0002480	0,0002000	0,0003680	0,0004490	0,0007310
	6					0,0002460	0,0001630	0,0003460	0,0004740
	7						0,0003090	0,0002070	0,0003690
	8							0,0003880	0,0002840
	9								0,0004750



B.5 References

- Fortescue P. and J. Stark, "Spacecraft Systems Engineering", ISBN 0471 95220 6, 1995. Flury W., "ELDO", ESRO Scientific and Technical Review, Vol. 5, RDB.1
- RDB.2
- Cook G.E., Geophysics Journal, Vol. 6, p.271, 1962. RDB.3



 $(This\ page\ is\ intentionally\ left\ blank)$



Annex C (informative)

Geomagnetic field

C.1 Description of magnetosphere

Figure C-1 shows a schematic of the magnetosphere, including representative field lines and the main "external" current systems. The impinging solar wind compresses the Earth's field on the day side and elongates it on the night side, making a bow-wave and wake type structure. Although the main Earth field is relatively stable, the external currents are highly variable and affected by solar wind and interplanetary magnetic field effects resulting from solar events such as high speed streams, coronal mass ejections and shocks.

The main external current systems are:

- the ring current, flowing azimuthally around the Earth in the plasmasphere $(L \leq 4)$;
- the cross-tail current;
- magnetopause boundary currents.

C.2 Derivation of dipole strength from field model coefficients

Considering the centred dipole terms (n = 1, m = 0,1), equation 5.1 then becomes:

$$V = \frac{1}{r^2} \left\{ g_1^0 a^3 \cos(\theta) + g_1^1 a^3 \cos(\phi) \sin(\theta) + h_1^1 a^3 \sin(\phi) \sin(\theta) \right\}$$

Each of the terms represents the contribution to the total dipolar potential from dipoles aligned with the three geocentric Cartesian axes. This is easily seen since the scalar potential due to a dipole whose strength and orientation are given by a moment m is:

$$V = \frac{(\underline{m}.\underline{r})}{r^3} = \frac{1}{r^2} \left\{ m_z \cos(\theta) + m_x \cos(\phi) \sin(\theta) + m_y \sin(\phi) \sin(\theta) \right\}$$

Comparing these equations it is clear that the total dipole strength (moment) is therefore:

$$M = a^{3} \left[(g_{1}^{0})^{2} + (g_{1}^{1})^{2} + (h_{1}^{1})^{2} \right]^{1/2}$$



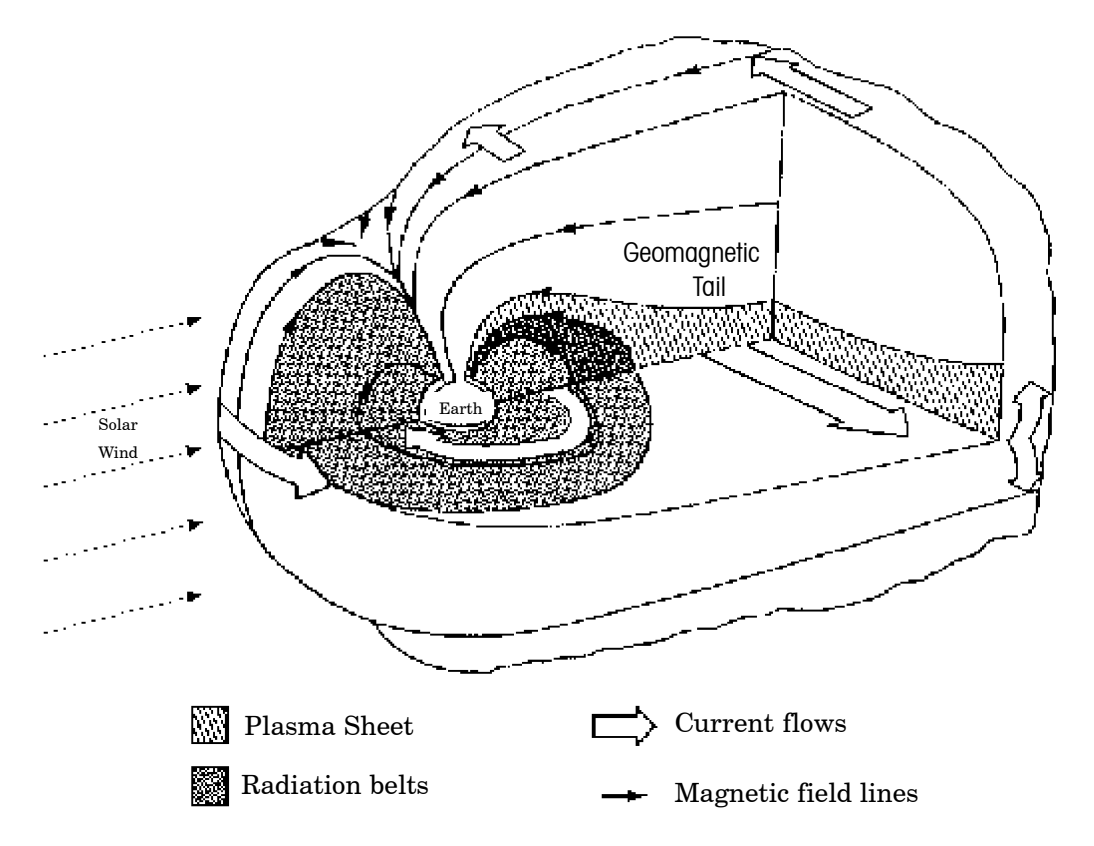


Figure C-1: Schematic of the magnetosphere showing the current flows and magnetic field lines

C.3 Incompatibilities and inconsistencies

McIlwain first established the B,L coordinate system in 1961 with a dipole moment of 31165,3 nT. R_E^3 [RD C.1]. This raises an important problem. Although changes to the geomagnetic field are small, they can have a large effect if applied to radiation environment models which have large gradients of particle flux as a function of altitudes, at their lowest altitudes [RD C.2] and so are highly susceptible to error. It is therefore important when computing B,L coordinates for accessing radiation environment models to use precisely the same definition of L (and therefore value for M in equation 5.2), together with the geomagnetic field model and epoch, as were used in the production of the model in the first place.

Vette [RD C.3] indicates that the Jensen and Cain model (epoch 1960) was used throughout this modelling. However, even this subsequently appears to be wrong [RD C.2]. Therefore, use of the models defined in clause 9, together with M=31165,3, shall be regarded as the standard for computing B,L for radiation environment models until provisions for employing more recent models can be made.

C.4 IGRF model details and availability

The formal contact point for the IGRF series models is:

IGRF Secretariat, NASA/GSFC, Code 921

Greenbelt, Maryland 20771

langel@geomag.gsfc.nasa.gov

However, the model is available via WWW or FTP at:

ftp://nssdc.gsfc.nasa.gov/pub/models/

and more information is available at:

http://nssdc.gsfc.nasa.gov/space/model/magnetos/



The IGRF-95 model consists of coefficient sets for the epochs 1945 to 1995 in steps of five years and the first time derivatives of the coefficients for the time period 1995 to 2000. During the 5-year intervals between consecutive models, linear interpolation is recommended. The IGRF coefficients for 1945, 1950, ... 1985, 1990 are definitive coefficient sets, referred to by the title DGRF.

In combination with the IGRF coefficient sets different subroutines have been used to determine the components of the magnetic field vector and the L-value at a given location. The standard version uses the subroutines FELDG (magnetic field vector) and SHELLG (L shell) developed by G. Kluge (ESA/ESOC). His use of inverse Cartesian coordinates simplifies the computation. The IGRF subroutines were developed by A. Zunde of the U.S. Geological Survey (USGS). The program BILCAL produces tables of the geomagnetic field strength, vector components ($B_{abs.}$, B_{north} , B_{east} , B_{down} , declination, inclination), equatorial/minimum field strength (B_0), dipole moment, and L-value in latitude, longitude (geodetic), altitude, or year (decimal).

Models referred to in clause 5 for the perturbations to the Earth field from external sources are available from the NSSDC www site (http://nssdc.gsfc.nasa.gov/space/model/).

Models and access routines are also available in Europe from BIRA/IASB (B) and via the WWW at http://www.spenvis.oma.be/spenvis, the Space Environment Information System.

C.5 References

- RDC.1 McIlwain C.E., "Coordinates for Mapping the Distribution of Geomagnetically Trapped Particles", J. Geophys. Res. 66, 3681 (1961).
- RDC.2 Lemaire J., E.J. Daly, J.I. Vette, C.E. McIlwain and S. McKenna-Lawlor, "Secular Variations in the Geomagnetic Field and Calculations of Future Low Altitude Radiation Environments", Proceedings of the ESA Workshop on Space Environment Analysis, ESA WPP-23, ESTEC/WMA, Noordwijk, The Netherlands, October 1990.
- RDC.3 Vette J.I., "The NASA/National Space Science Data Center Trapped Radiation Environment Model Program (1964–1991)", NSSDC WDC-R&S Report 91–29, p.21, NASA-GSFC-NSSDC, November 1991.



 $(This\ page\ is\ intentionally\ left\ blank)$



Annex D (informative)

Solar and Earth electromagnetic radiation and indices

D.1 Solar spectrum details

Figure D-1 shows the solar irradiation spectrum at sea level and outside the Earth atmosphere.

Solar irradiance values (in photons/cm 2 s $^{-1}$) and energy fluxes (in W/cm 2) for the wavelength range 175,439 nm to 852,5 nm, split into small intervals, are given in [RDD.1] and reproduced in [RDD.2].

The ASTM standard [RDD.3] defines a solar spectral irradiance curve for the wavelength range $115\ nm$ to $400\ 000\ nm$.

D.2 Albedo and infrared variability

Information on the variability of the albedo and the Earth infrared radiation can be found in [RDD.2].

As an example, Table D-1 gives the mean albedo data for 30° , 60° and 90° inclination orbits. These are average values taken from [RDD.2]. The average albedo from Table D-1 (and also the average from other, more extensive data, given in [RDD.2]) appears to be somewhat below the standard average value of 0,3.

The values are the reflected fraction. The given percentile is the probability that the indicated albedo value is not exceeded. The albedo values are corrected to zero zenith angle.

Table D-1: Running mean (averaged over 90 minutes) albedo percentile data

Orbit Incl.	3 %	50 %	97 %
30°	0,14	0,18	0,22
60°	0,17	0,23	0,32
90°	0,18	0,25	0,34

A value of 0.3 and the same spectrum as the Sun were specified as standard for the Earth albedo. On a short time scale, albedo can be very variable and range from about 0.05 to 0.6.



In addition, the albedo spectrum can change, depending on properties of the surface and atmosphere. Ground vegetation and atmospheric water and dust can lead to absorption in certain wavelength bands and result in a highly variable albedo spectrum.

Table D-2 gives running mean values for the Earth emitted infrared radiation for 30° , 60° and 90° inclination orbits. These are average values taken from [RDD.2]. The given percentile is the probability that the indicated infrared radiation value is not exceeded.

Table D-2: Running mean (averaged over 90 minutes) Earth infrared radiation percentile values in units of W/m²

Orbit Incl.	3 %	50 %	97 %
30°	227	246	265
60°	211	233	255
90°	205	227	250

D.3 Activity indices information

Figures D-2 and D-3 show the $F_{10,7}$, Sunspot Number (SSN) and A_p indices over the last two solar cycles. Figure D-2 gives the daily and Figure D-3 the monthly mean values. The large fluctuations in the daily values are averaged out in the monthly mean values (please note the different scale of the figures). The short term A_p spikes are important for density variations and this is not well reflected in the long term high values.

The long term predictions of average solar activity, as given in Table 11 (see clause 6) can bias by mild cycles. The solar activity of the last two cycles clearly exceeded the long term average.

Regular updates of measured and predicted activity values are provided by the Marshall Space Flight Center [RDD.4a] and the National Geophysical Data Center [RDD.4b]. Indices are available via the World Wide Web:

http://www.ngdc.noaa.gov/

D.4 Radio noise

The magnetosphere-ionosphere system is filled with natural plasma emission sources. Fig. D.4 presents an overview of the natural plasma noise levels from near-Earth, solar and some cosmic sources (taken from [RDD.2]).

Electromagnetic radiation with frequencies below the peak plasma frequency of 1 MHz to 10 MHz is most likely negligible for spacecraft if the source is below about 200 km. The main near-Earth noise sources above that altitude are auroral arcs and ionospheric irregularities.

Man-made narrow band sources from 1 MHz to 300 GHz can be important for orbiting spacecraft.

D.5 Solar radiation pressure

A spacecraft moving within the solar system experiences a perturbation to its trajectory due to the incidence of solar radiation upon its illuminated surfaces. Electromagnetic radiation carries momentum and the reflection of incident radiation at a surface represents an exchange of momentum. The solar radiation exerts a small pressure, SRP, on a spacecraft given by:

$$SRP = \frac{F}{c}$$

where F is the solar energy flux at the spacecraft and c is the speed of light.



The effect of this solar radiation pressure as a force acting upon the vehicle is dependent upon the reflective characteristics of the spacecraft surfaces.

The perturbing effect upon a spacecraft's trajectory is directly dependent upon the vehicle's area to mass ratio and inversely proportional to the square of its distance from the Sun.

Hence the disturbing acceleration due to solar radiation F_{SRP} , acting along the Sun-spacecraft line, can be expressed as:

$$F_{SRP} = R \frac{A}{m} SRP \left(\frac{a_s}{r_s}\right)^2$$

where

 ${\it R}$ is a constant whose value depends upon the reflective properties of

the surface;

 r_s is the distance of the satellite from the Sun;

 a_s is the mean distance of the Earth from the Sun;

A is the area of the satellite;m is the mass of the satellite.

D.6 Figures

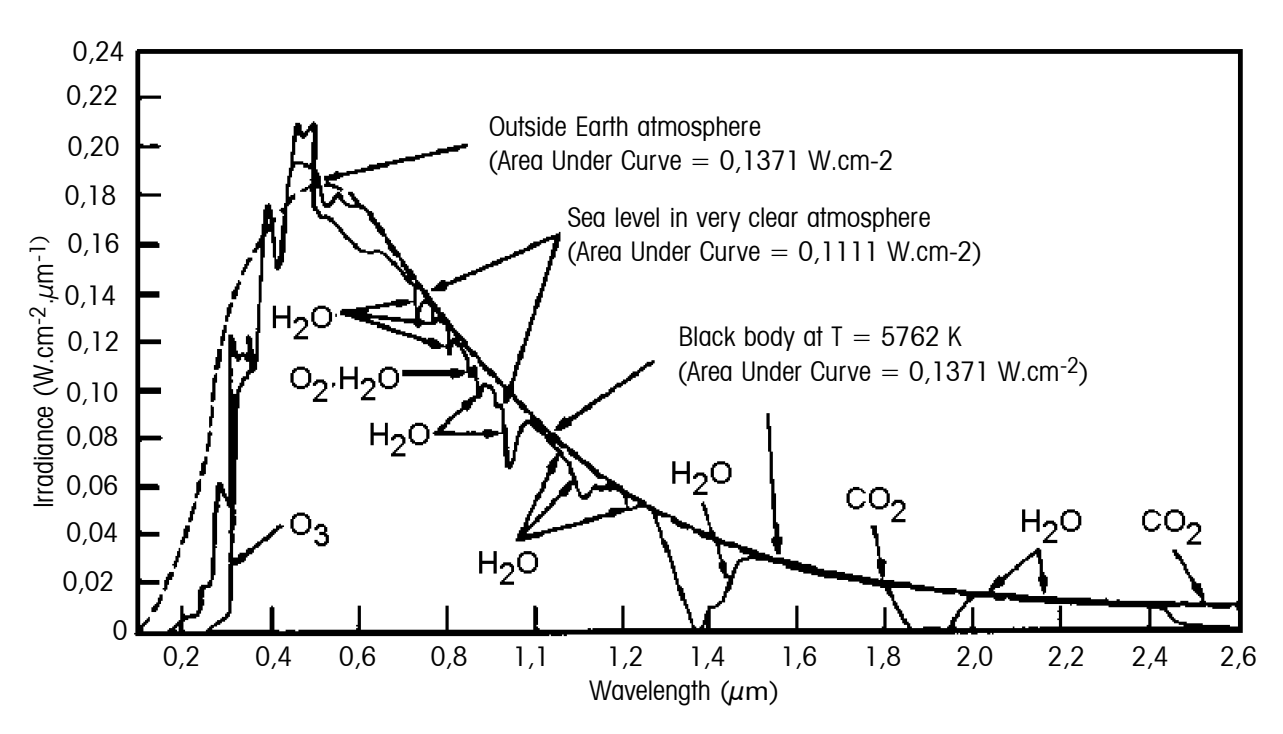


Figure D-1: Normally incident solar radiation at sea level on very clear days, solar spectral irradiance outside the Earth atmosphere at 1 AU, and black body spectral irradiance curve at T=5762 K.



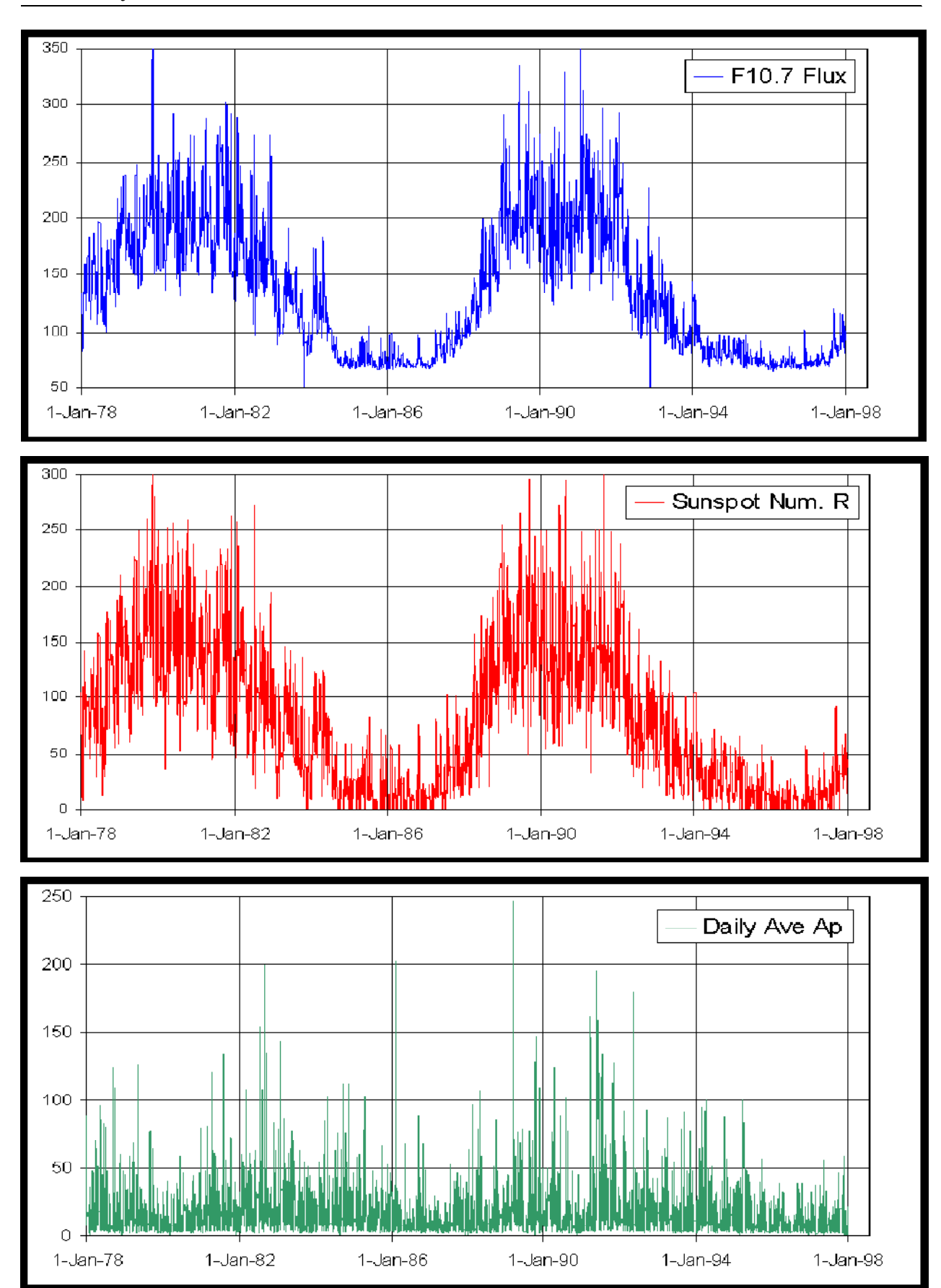


Figure D-2: Daily solar and geomagnetic activity indices over the last two solar cycles.



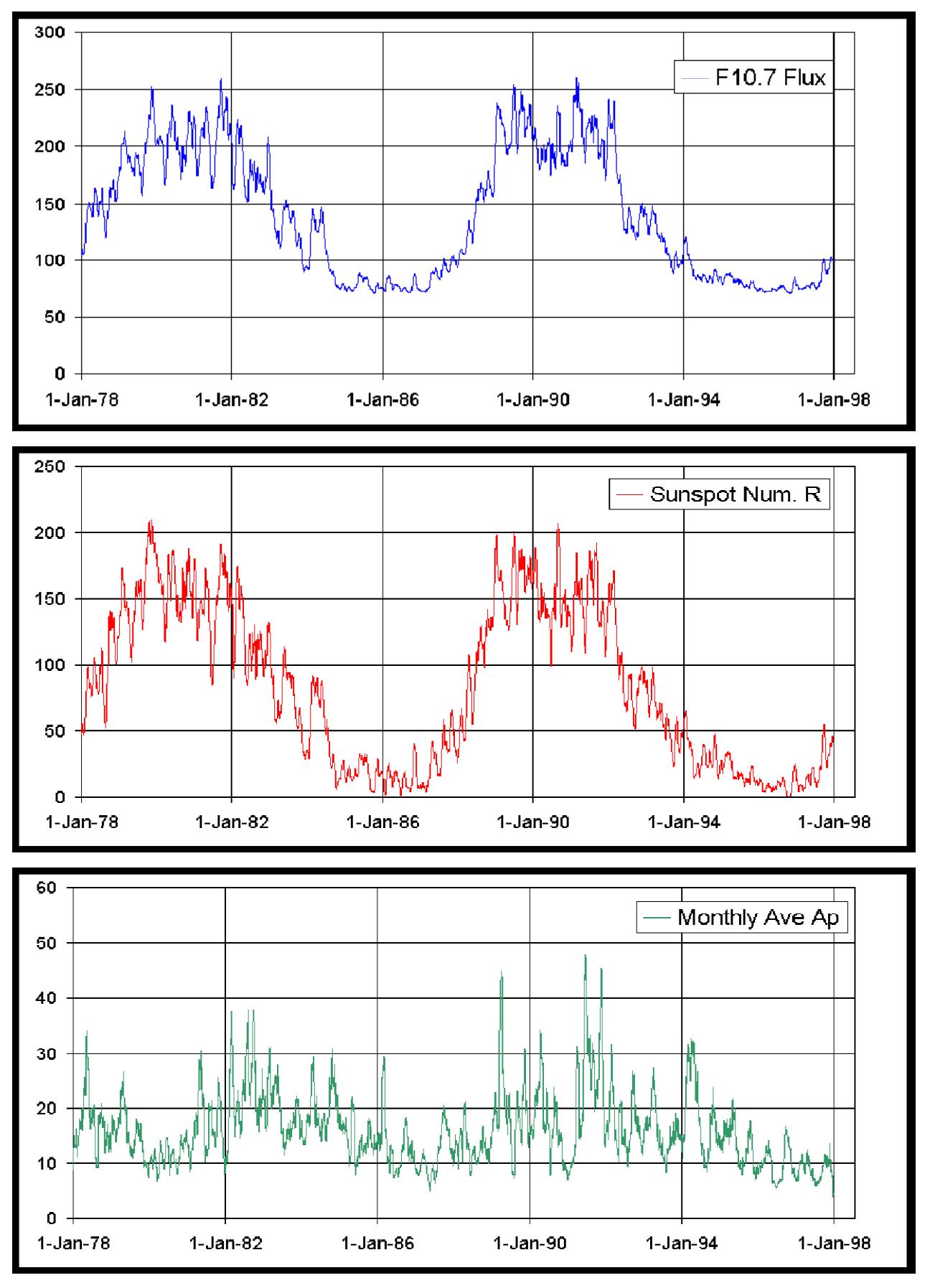


Figure D-3: Monthly mean solar and geomagnetic activity indices over the last two solar cycles.



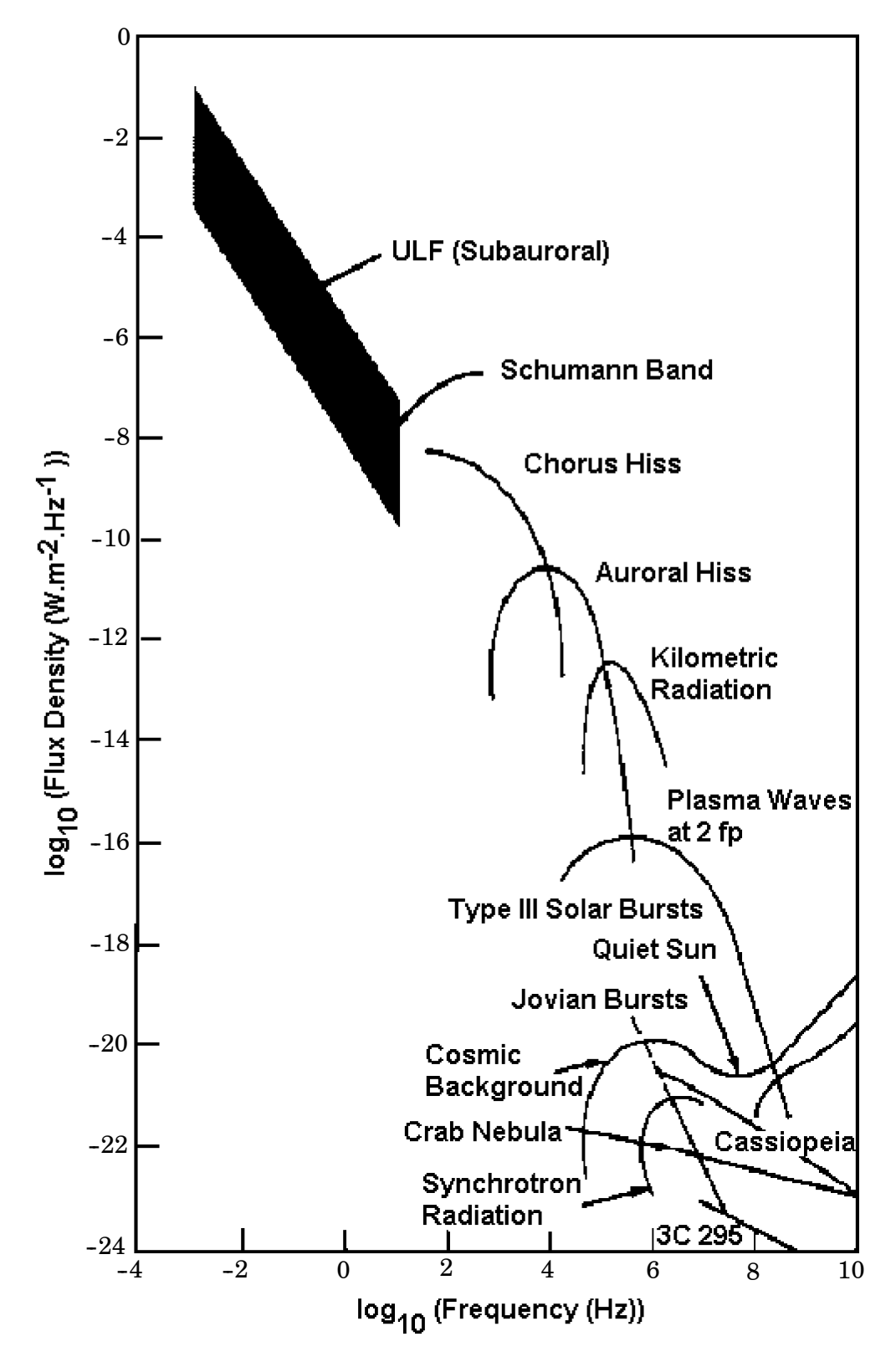


Figure D-4: Power flux levels for various frequency ranges of naturally occurring electromagnetic and plasma waves (from [RDD.2]).



D.7 References

- RDD.1 World Meteorological Organization, Compiler: "Atmospheric Ozone 1985, Assessment of Our Understanding of the Processes Controlling Its Present Distribution and Change", World Meteorological Organization Report, No. 16, Vol.1 Chapter 7, 1985.
- RDD.2 "Natural Orbital Environment Guidelines for Use in Aerospace Vehicle Development", B.J. Anderson, editor and R.E. Smith, compiler; NASA TM 4527, Chapters 6 and 9, June 1994.
- RDD.3 "Standard Solar Constant and Air Mass Zero Solar Spectral Irradiance Tables", American Society for Testing and Materials, ASTM standard E 490-73a (Reapproved 1992).
- RDD.4 a) "Solar Activity Inputs for Upper Atmospheric Models", George C. Marshall Space Flight Center, Updates of measured and predicted activities are distributed monthly.
 - b) Weekly measurements of solar and geomagnetic activity levels are published by the National Geophysical Data Center, Boulder.



 $(This\ page\ is\ intentionally\ left\ blank)$



Annex E (informative)

The neutral Earth atmosphere

E.1 Overview of atmosphere models

Early models of the thermosphere emerged around 1965 (e.g. Harris-Priester, Jacchia-65). These, as well as their descendants Jacchia-71 [RDE.1], CIRA-72 [RDE.2], and Jacchia-77 [RDE.3], were based on a numerical quadrature of the species-wise diffusion equations. In these models the altitude profile of the number densities n_i is largely determined by the magnitude of the exospheric temperature T_{∞} . This quantity is used to accommodate all activity related and diurnal effects, while semi-annual variations are introduced via empirical correction functions. In the Jacchia-77 model species-wise corrections are also introduced for diurnal, seasonal/latitudinal, and geomagnetic effects. The numerical quadrature can be very CPU demanding in orbit predictions. To improve the turn around time for calls to such routines, Mueller [RDE.4] implemented the Jacchia-Lineberry algorithm for the Jacchia-71 [RDE.1] model, and Lafontaine [RDE.5] developed an equally efficient method to approximate the Jacchia-77 model. The MET-87 model (Marshall Engineering Thermosphere Model, [RDE.6]) is also based on the early Jacchia-71 atmosphere, but it extends the range of output quantities, including pressure, pressure scale height, and ratio of specific heats.

Another line of atmosphere models directly applies analytical solutions of simplified diffusion equations to derive concentration profiles. The most prominent class of these models is called MSIS (Mass Spectrometer and Incoherent Scatter, [RDE.7, RDE.8, RDE.9]).

The MSIS models were continuously improved in 1977, 1983, and 1986 as new measurement data and new analysis results became available. MSIS-86 also became the CIRA-86 reference atmosphere for thermospheric altitudes. Recently, MSIS 86 has been upgraded to MSISE-90 by a continuation to ground level with smooth density and temperature profiles. The DTM-77 model (Density and Temperature Model) by Barlier et al. has a similar structure as MSIS-77 but limits itself to the constituents N_2 , O_2 , O_3 , and O_3 and O_3 are into account. The C model by Proelss et al. [RDE.10, RDE.11]. Hydrogen, which becomes dominant at high altitudes especially for low activity levels, is not taken into account. The C model by Proelss et al. [RDE.12] also has a MSIS-77 structure with modified correction functions. The advantage of MSIS, DTM, and O_3 lies in their model flexibility to account for observed changes, and in their comprehensive range of output results (including number densities).



A third class of thermosphere models only aims at total densities as output result. The underlying data of the Russian GOST-84 model [RDE.13] are solely derived from satellite drag analysis. Total density is computed from a reference altitude profile which is adjusted by four factors accounting for (1) diurnal, (2) seasonal/latitudinal, (3) solar activity, and (4) geomagnetic activity effects. An updated set of model coefficients has been published in 1990. The TD-88 model by Sehnal et al. [RDE.14] is more flexible in its formulation, since TD-88 does not assume a rigorous separation of perturbing effects (factorization of corrections) as is done by GOST-84. The TD-88 model, however, should only be applied to altitudes from 150 km to 750 km.

E.2 Accessibility of the MSISE-90 model

The MSISE-90 model can be obtained via "ftp://nssdc.gsfc.nasa.gov/pub/models/msise90" from the NSSDC Web homepage. In applications which require a smooth, continuous density profile with altitude the "departure from diffusive equilibrium" option in MSISE-90 should be switched off (corresponding to switch setting SW(15) = 0.0).

E.3 References

- RDE.1 Jacchia L.G., "Revised Static Models of the Thermosphere and Exosphere with Empirical Temperature Profiles", SAO Report No. 332, May 5, 1971.
- RDE.2 anon., "CIRA-72 (COSPAR International Reference Atmosphere 1972)", Akademie Verlag, Berlin, 1972.
- RDE.3 Jacchia L.G., "Thermospheric Temperature, Density, and Composition New Models", SAO Report No. 375, March 15, 1977.
- RDE.4 Mueller A., "Jacchia-Lineberry Upper Atmosphere Density Model", NASA Report 82-FM-52/JSC-18507, Oct. 1982.
- RDE.5 Lafontaine J. de and P. Hughes, "An Analytic Version of Jacchia's 1977 Model Atmosphere", Celestial Mechanics 29 (1983), pp 3–26, 1983.
- RDE.6 Hickey M.P., "The NASA Marshall Engineering Thermospheric Model", NASA CR-179359, July 1988.
- RDE.7 Hedin A.E., "MSIS-86 Thermospheric Model", J. Geophys. Res., Vol. 92, No. A5, pp 4649-4662, May 1, 1987.
- RDE.8 Hedin A.E., "Extension of the MSIS Thermosphere Model into the Middle and Lower Atmosphere", J. Geophys. Res., Vol. 96, No. A2, pp. 1159-1172, Feb. 1, 1991
- RDE.9 Hedin A.E. et al., "Revised Global Model of Thermosphere Winds Using Satellite and Ground-Based Observations", J. Geophys. Res., Vol. 96, No. A5, pp. 7657-7688, May 1, 1991
- RDE.10 Barlier F., C. Berger, J.L. Falin, G. Kocharts and G. Thuiller, "A Thermospheric Model Based on Satellite Drag Data", Aeronomica Acta A-No. 185, 1977.
- RDE.11 Koehnlein W. et al., "A Thermospheric Model of the Annual Variations of He, N, O, N₂ and Ar from AEROS Nims Data", J. Geophys. Res., Vol. 84, pp. 4355-4362, 1979.
- RDE.12 Proelss G.W. and Blum P.W., "Comparison of Recent Empirical Models of the Thermosphere", in Proceedings of ESA workshop on Re-Entry of Space Debris, Darmstadt, 24–25 September 1985 (ESA SP-245)
- RDE.13 anon., "Density Model for Satellite Orbit Predictions", GOST 25645-84, Standards Editing House, Moscow, 1984.
- RDE.14 Sehnal L. and L. Pospisilova, "Thermospheric Model TD 88", Preprint No. 67, Observatory Ondrejov, 1988.



Annex F (informative)

Plasma

F.1 Surface charging

This is principally a phenomenon that occurs in the outer magnetosphere, where plasma temperatures are high, but can also occur in the auroral zone, due to high fluxes of precipitating energetic electrons. High-level electrostatic charging results from the tendency for surfaces to achieve an equilibrium where there is a balance of the currents to them:

$$I_e + I_p + I_{se} + I_{be} + I_{sp} + I_{ph} + I_{cond} = 0$$

where

 I_e is the electron ambient current. This is the driver of high-level charging to negative potential;

 I_p is the ion ambient current. This counters negative charging but is weaker than electron current, since flux is proportional to $(KT/M)^{1/2}$;

 I_{se} is the low-energy secondary electrons resulting from electron impact. This is strongly material-dependent. Yield can be > 1 for low-energy impacting electrons;

 I_{be} is the back-scattered primary electrons;

 I_{sp} is the low-energy secondary electrons resulting from ion impact;

 I_{ph} is the low-energy photoemitted electrons due to solar UV. This is usually the dominant counter-charging current in sunlight;

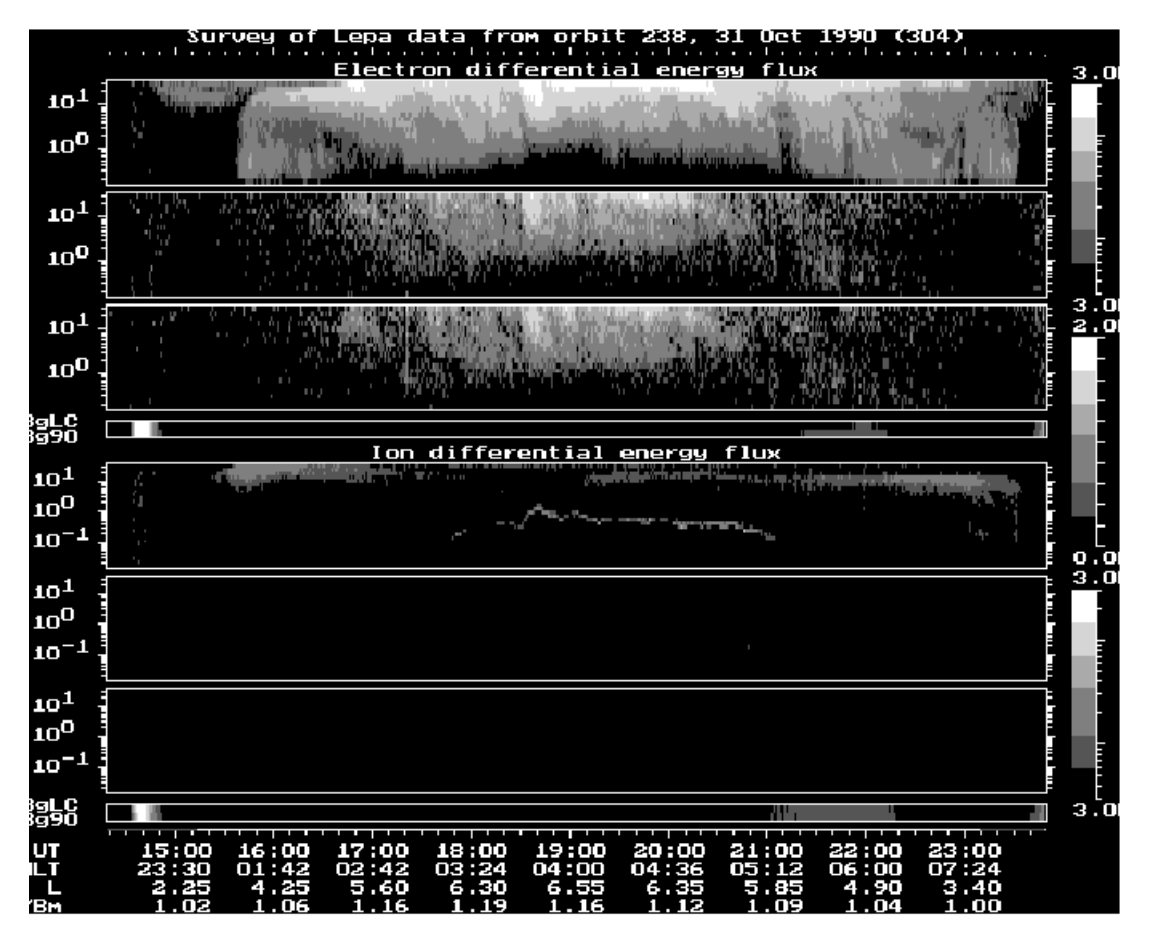
 I_{cond} is the current between spacecraft surfaces, via material resistivity.

Charging occurs when I_e dominates the other currents. The surface potential becomes increasingly negative until this current becomes diminished by the potential barrier and equality with the other currents is achieved. Because secondary emission, back-scatter, photoemission and conductivity all depend on material properties, the flux and spectrum of the incident electrons, required to cause charging, depend on the material. The secondary emission coefficient (σ) is crucial, peaking usually for incident electrons of energy < 1,5 keV. If σ is greater than one, the net electron current opposes charging. At higher-energy the yield falls and as a result, the higher-energy component of the environment is important in driving charging. In sunlight, a surface emits a high flux of low-energy electrons which opposes charging. Darkness, due to satellite eclipse or self-shadowing, removes this photoelectron emission and high-level charging is more likely in these conditions.



Charging of a whole spacecraft is not usually hazardous, although it can interfere with the operation of scientific instruments. Danger to the spacecraft itself usually results from differential charging i.e. where different parts of the spacecraft are charged to different levels. This occurs because of the different material characteristics and orientation of different surfaces. The resulting electrostatic discharges between adjacent surfaces or between surfaces and ground can cause current spikes in sensitive electronic circuitry.

Figure F-1 shows a charging event as detected by the Low Energy Plasma Analyser on CRRES. The narrow band in the top ion spectrogram, between 18 UT and 21 UT, corresponds to cold ions that are accelerated into the detector by the spacecraft potential. On this occasion, the spacecraft potential reached more than 1 kV. This occurred when electron fluxes above 10 keV were most enhanced.



The three frames for each species correspond to look directions perpendicular to the field, field-aligned (looking equator-ward) and field-aligned (looking Earth-ward). (Courtesy of MSSL/UCL)

Figure F-1: Spectrograms showing electron and ion fluxes during a charging event

F.2 Charging in LEO

Charging in LEO occurs for the same reasons as charging elsewhere, i.e. due to high fluxes of electrons with energy a few kilo electron-volts or higher. This limits LEO charging to the auroral zone. However, at low altitudes, there is a substantial cold ion population which tends to neutralize negative potentials. Hence charging occurs less readily, and preferentially on wake surfaces, where ion densities are reduced. It rarely achieves the potentials seen in the outer magnetosphere but causes a greater amount of sputtering due to the high ion density.



Figure F-2 shows the charging potential seen during an auroral crossing by DMSP F6 in November 1983. The spacecraft potential showed little correlation with electron total flux but peaked when electron fluxes above 14 keV were high.

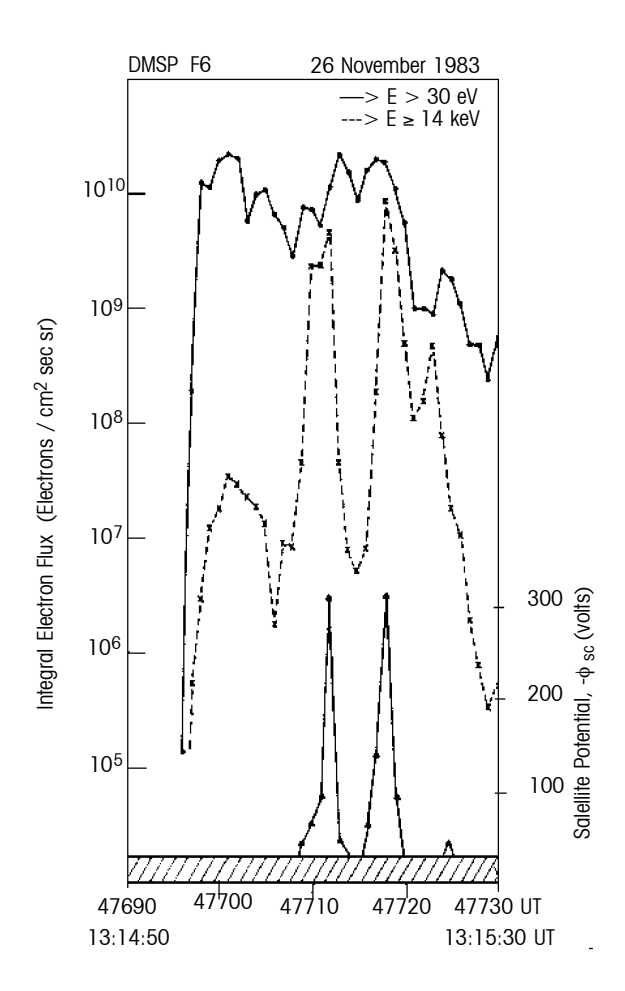


Figure F-2: Satellite potential and electron integral number flux above 30 eV and 14 keV [RDF.1]

Yeh and Gussenhoven [RDF.2] performed a statistical survey of environments seen by the DMSP satellite and their relationship with LEO charging levels. Various models are given, corresponding to different observed spectral shapes and reflecting the origin of the electrons:

- Type 1: low-energy Maxwellian + accelerated Maxwellian;
- Type 2: constant at low-energy + accelerated Maxwellian;
- Type 3: double-exponential + accelerated Maxwellian.

About 50 % of the >100 V charging events corresponded to type 2 and this is the type of spectrum adopted by MIL-STD-1809 [RDF.3] and used in this Standard. The transition between low and high-energy parts is at energies in the range $12-18~\rm keV$ and the accelerated Maxwellian has temperatures of $4-7~\rm keV$.

F.3 NASCAP charging code

The most commonly used code in the West, for simulating surface charging in the outer magnetosphere, is NASCAP or NASCAP-GEO [RDF.4]. This calculates the total current, due to all the current contributions, for each surface on a numerically modelled 3-D spacecraft, using a two Maxwellian environment for both ions and electrons. From these currents, the change in potential at each surface is calculated. The current and potential calculations can be performed iteratively until an equilibrium charging state is achieved. Where spacecraft geometry is



unimportant because all that is required is the susceptibility of a particular material to charging in a particular environment, then a simple 1-D code, MATCHG [RDF.4], based on a subset of NASCAP subroutines, can be used. Current collection in both codes is determined using the "thick sheath" approximation i.e. assuming that the Debye length is long compared to the spacecraft dimensions. This approach is valid at GEO but for charging in low-altitude auroral conditions a different approach is needed.

In Figure F-3, MATCHG has been used to show the different charging responses to changing electron temperature of a number of typical materials found in space. Each is for a single Maxwellian distribution with density 1 cm⁻³, in eclipse. For each material, the potential rises with electron temperature but the different secondary emission characteristics means that there is a wide difference between different materials.

Ion and electron density of 1 ${\rm cm}^{-3}$ is assumed and an ion temperature of 10 keV. For each material the secondary yield maximum and the energy at which it occurs is given.

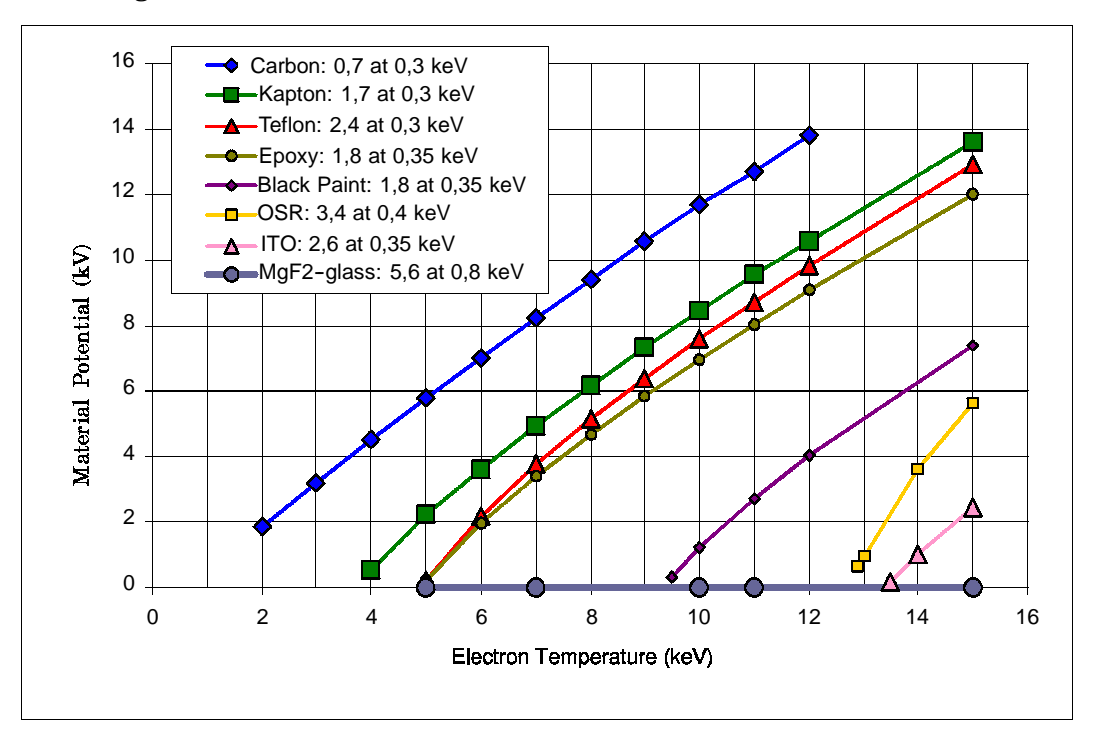


Figure F-3: Surface potential vs. electron temperature for a number of materials

F.4 POLAR charging code

The main problem with computing charging in LEO is computing effects associated with the spacecraft sheath. The most notable computational tool for assessing interactions and charging at low altitudes is the 3-D POLAR code [RDF.5]. This uses numerical techniques to track ambient ions inwards from the electrostatic sheath surrounding a negatively charged spacecraft, onto the spacecraft surface. Spacecraft velocity is included as an input and ram and wake effects are simulated. One or two Maxwellian components may be used to define the ambient plasma. The electron population in POLAR is a superposition of power-law, Maxwellian, and Gaussian components. Once the surface currents have been found, POLAR calculates potentials and equilibrium charging state in a similar way to NASCAP.



F.5 Other charging codes

There are a number of other codes available to simulate surface charging. Two Russian codes ECO-M [RDF.6] and COULOMB [RDF.7] perform a very similar function to NASCAP and POLAR and a LEO version of NASCAP, called NASCAP-LEO [RDF.8] also exists. A 1-D charging code, called EQUIPOT [RDF.9] performs computations assuming either thick-sheath or thin-sheath current collection and is thus applicable to GEO and LEO charging.

This code is available in the Space Environment Information System (Spenvis) at http://www.spenvis.oma.be/spenvis/.

Whilst charging codes are usually a good indicator of whether a spacecraft design is susceptible to charging or not, it is very difficult to quantitatively calculate charging potentials. The main reason for this is that the equilibrium potential is highly sensitive on material properties, such as secondary emission coefficient. These properties are very difficult to measure on the ground and, in any case, frequently change in orbit.

F.6 NASA worst case charging environment

The NASA worst case charging environment for the outer magnetosphere [RDF.10] is widely used in spacecraft charging assessment and is different from the one defined in this standard. NASA chose a worst case charging event derived from the 90th percentile ion and electron environments.

Table F-1: NASA worst-case environment

Ne (cm ⁻³⁾	Te (KeV)	Ni (cm ⁻³⁾	Ti (KeV)
1,12	12	0,236	29,5

Since severe ion and electron environments do not necessarily happen at the same time it is felt that this environment is overly severe. Hence in this standard, an extreme environment, known to produce severe charging has been specified.

F.7 Ram and wake effects

When a spacecraft velocity is higher than or comparable to the ion acoustic velocity, it distorts the plasma environment it experiences, creating a void of particles behind it and often a build-up of particles before it. These effects are seen principally in the ionosphere. The ion acoustic velocity is the speed at which pressure differences are transmitted through a plasma and is defined as:

$$V_s = \left(\frac{KT_e + \gamma kT_i}{M}\right)^{1/2}$$

where

 V_s is the acoustic velocity in m s⁻¹;

k is the Boltzmann constant;

 T_e and T_i are the electron and ion temperatures, respectively, in K;

M is the ion mass in kg; γ is a constant, usually 3.

Taking typical parameters for the 300 km ionosphere ($T_e = T_i = 1000$ K, Composition 77 % O+, 20 % H+, 3 % He+) this velocity is 1,5 km/s. A spacecraft in a circular orbit at this altitude has a velocity V of 7,7 km/s. Hence the spacecraft motion is supersonic. As the spacecraft moves through the plasma it sweeps up particles ahead of it and the plasma is too slow to fill in the void behind it as soon as it passes by. The result is that there is a wake behind the spacecraft with essentially none of the local cold plasma in it. The length of the wake depends on the Mach number



 V/V_s of the spacecraft and its width. In the ram direction, density can be enhanced by back-scattering of ions from the front of the spacecraft.

Wake creation can be used to create an extremely pure vacuum for materials processing in space. It is also a means for creating charging conditions in low Earth orbit because potentials created by energetic auroral electrons are not neutralized by the ambient ions. Under these conditions the wake can become very complex because ion trajectories can be bent and accelerated by the potential, partially filling the wake. The resulting intense flux of ions can increase erosion by sputtering.

F.8 Current collection effects

In the ionosphere, the intense plasma density means there is an ample supply of ions and electrons which tend to neutralize high potential surfaces on spacecraft. However, on solar panels, high potentials are maintained by the action of sunlight on photovoltaic cells. In this case, the incident ions and electrons, collected on the negative and positive ends of the solar array respectively, act as a current travelling through the ionospheric plasma. This current is hence not available to drive spacecraft systems and so the efficiency of the solar panels is effectively diminished.

The different mobilities of the ions and electrons means that electrons are collected more easily than ions. This drives the positive end of the array towards space potential and leaves the negative end at high negative potential. The precise potentials at equilibrium depend on the exposed areas on the array and on the rest of the spacecraft. The grounding strategy of a spacecraft can be very important in determining spacecraft potential under these circumstances. If spacecraft ground is attached to the positive end of the array, it floats at a small positive potential. If it is attached to the negative end, it floats at a negative potential, which depends on the collecting area but which is generally a high fraction of the total potential across the solar array. This situation can be quite hazardous, as it increases the possibility of arcing between ground and insulated surfaces and leads to enhanced sputtering by impacting ions. A study of grounding strategy on Space Station Freedom [RDF.11] showed that a total array potential difference of 160 V results in structure ground being between -115 V and -150 V, if the structure were negatively grounded. The study showed that this situation can be corrected by use of a plasma contactor, emitting a sufficiently high current of elec-

F.9 Sputtering

Sputtering is the removal of surface material by the impact of ions. Where thin surface coatings are used, this can significantly alter surface characteristics over time and produces a contaminant population which may adhere to other surfaces. The overwhelming majority of sputtered products are neutral atoms, although 2 %–4 % may be emitted as ions. In the ionosphere, the spacecraft ram velocity can cause significant sputtering due to the dense ion and neutral population, even though the yield per impact can be very low (around 10^{-6} [RDF.12]). Sputtering is expected to be considerably enhanced when high spacecraft potential, caused by spacecraft charging or an inappropriate grounding strategy, causes cold ionospheric ions to be accelerated onto the spacecraft surface. Peak yields are generally higher for higher atomic number ions and occur at higher energies. For He $^+$ on Al, the yield peaks just below 1, at 1 keV [RDF.13].

In the outer magnetosphere, where charging events are more common, sputtering has been observed to produce a small contaminant ion population [RDF.14]. The high flow velocity of the solar wind gives a proton a kinetic energy of typically 1,5 keV, is expected to give significant sputtering rates in this region too. A comprehensive theory for how sputtering occurs is given by Sigmund [RDF.15] and



Thompson [RDF.16]. Irrespective of the incident ion species or energy, the sputtered atoms have energies of about 10 eV [RDF.13].

F.10 Ionospheric propagation effects

The most significant propagation effect of the ionosphere is the reflection of waves below a critical frequency, called the plasma frequency, so that communications between ground-stations and spacecraft shall take place at higher frequencies. The plasma frequency is a function of electron density, as described below and is typically between 1 MHz and 9 MHz.

$$f_{\scriptscriptstyle p} = rac{1}{2\pi} iggl(rac{N_{\scriptscriptstyle e} e^2}{arepsilon_0 m_{\scriptscriptstyle e}}iggr)^{1/2} \quad {
m or} \quad f_{\scriptscriptstyle p} = 9 N_{\scriptscriptstyle e}^{1/2}$$

where

 f_p is the plasma frequency in s⁻¹; N_e is the electron density in m⁻³;

 ε_0 and m_e are natural constants.

For high-accuracy positioning of radio beacons by range or range rate measurement between a satellite and a ground-based beacon and for radar altimetry, the propagation delay caused by ionospheric plasma density shall be considered to achieve accurate range measurements. This delay can be expressed as:

$$\Delta T = -\frac{4,03 \times 10^3 N}{cf^2}$$

where

 ΔT is the propagation delay in seconds;

N is the electron column density along the path in m⁻²;

c is the velocity of light; f is the frequency in s^{-1} .

Since the models described in this Standard do not reflect time variations in ionospheric density, altitude corrections for radar altimetry purposes are, in practice, usually made by comparing radio propagation delays at two frequencies. The change in propagation speed of radio waves also means that refraction needs to be considered when calculating satellite orbits by radio tracking.

Below 300 MHz degradation of radio signals can occur, principally due to scintillation caused by ionospheric irregularities. Other propagation effects are dispersion, absorption and Faraday rotation.

F.11 Availability of the IRI95 model

The International Reference Ionosphere $95\,[RDF.17\,,RDF.18]$ can be obtained via the World-Wide Web at:

ftp://nssdc.gsfc.nasa.gov/pub/models/ionospheric/iri/iri95/

It can also be obtained on 2 floppy disks from the National Space Science Data Center request office by sending a request to:

request@nssdca.gsfc.nasa.gov

or by contacting:

NSSDC COSPAR/ URSI Working Group on IRI NASA/GSFC Code 933 Greenbelt MD 20771 U.S.A.



IRI facilities are also available through the Space Environment Information System (Spenvis) at http://www.spenvis.oma.be/spenvis

F.12 References

- RDF.1 Gussenhoven, D.A. Hardy, F. Rich, W.J. Burke and H.C. Yeh "High-Level Spacecraft Charging in the Low-Altitude Polar Auroral Environment" J. Geophys. Res., pp.110099-11023, 1985.
- RDF.2 Yeh H.C. and M.S. Gussenhoven "The statistical Electron Environment for Defence Meteorological Satellite Program Eclipse Charging", J. Geophys. Res., pp. 7705-7715, 1987.
- RDF.3 "Space Environment for USAF Space Vehicles", MIL-STD-1809 (USAF), 15 Feb 1991.
- RDF.4 Katz I., J.J. Cassidy, M.J. Mandell, G.W. Schnuelle, P.G. Steen and J.C. Roche, "The Capabilities of the NASA Charging Analyzer Program", in "Spacecraft Charging Technology 1978", Ed. R.C. Finke and C.P. Pike, NASA CP-2071/AFGL TR-79-0082, ADA045459, p. 101, 1979.
- RDF.5 Lilley J.R., Cooke D.L., G.A. Jongeward and I. Katz "POLAR User's Manual", AFGL-TR-85-0246.
- RDF.6 Vasilyev Ju.V, V.V. Danilov, V.M. Dvoryashin, A.M. Kramrenko and V.S. Sokolv, "Computer Modeling of Spacecraft Charging Using ECO-M", Proc. International Conference of Problems of Spacecraft/Environment Interactions, June 15-19, 1992 Novisibirsk, Russia, p.187, 1993.
- RDF.7 Krupnikov K.K, V.N. Mileev, L.S. Novikov and G.V. Babkin, "Mathematical Modelling of High Altitude Spacecraft Charging", Proc. International Conference of Problems of Spacecraft/Environment Interactions, June 15–19, 1992 Novisibirsk, Russia, p.167, 1993.
- RDF.8 Mandell M.J, I. Katz and D.L. Cooke, "Potentials on large spacecraft in LEO", IEEE Trans. Nucl. Sci. NS-29, p.1584, 1982.
- RDF.9 Wrenn G.L. and A.J. Sims, "Surface Potentials of Spacecraft Materials", Proc. ESA Workshop on Space Environment Analysis, p.4.15, ESA WPP-23, 1990.
- RDF.10 NASA TM 4527 "Natural Orbital Environmental Guidelines for Use in Aerospace Vehicle Development", Eds. B.J. Anderson and R.E. Smith, 1994.
- RDF.11 Hastings D.E., M. Cho and J. Wang, "Space Station Freedom Structure Floating Potential and the Probability of Arcing", J. Spacecraft and Rockets, vol.29, p.830, 1992.
- RDF.12 Hanson W.B., S. Santoni and J.H. Hoffman, "Ion Sputtering from Satellite Surfaces", J. Geophys. Res., 86, p.11350, 1981.
- RDF.13 Olsen R.C. and C.W. Norwood, "Spacecraft-Generated Ions", J. Geophys. Res., 96, 15951-15962, 1991.
- RDF.14 Olsen R.C. and E.C. Whipple, "An unusual charging event on ISEE1", J. Geophys. Res., 93, p.5568, 1988.
- RDF.15 Sigmund P., "Theory of Sputtering", Phys. Rev. Lett., 184, 383-416, 1969.
- RDF.16 Thompson M.W., "The energy spectrum of atoms during the high energy sputtering of gold", Philos. Mag, 18, 377-414, 1968.
- RDF.17 Bilitza D, "International Reference Ionosphere 1990", NSSDC/WDC-A-R&S 90–22, 1990.
- RDF.18 http://nssdc.gsfc.nasa.gov/space/model/ionos/iri.html



Annex G (informative)

Radiation

G.1 Links with radiation testing

Table G-1 below recalls the parameter used for quantification of various radiation effects, and for illustration purposes, lists the types of testing which shall be done to verify compatibility with the effects. See ECSS-E-20 for further details.

Table G-1: Radiation tests

Radiation effect	Parameter	Test means
Electronic component degradation	Total ionizing dose	Radioactive sources (e.g. ⁶⁰ Co), particle beams (e ⁻ , p ⁺)
Material degradation	Total ionizing dose	Radioactive sources (e.g. ⁶⁰ Co), particle beams (e ⁻ , p ⁺)
Material degradation (bulk damage)	Non-ionizing dose (NIEL)	Proton beams
CCD and sensor degradation	Non-ionizing dose (NIEL)	Proton beams
Solar cell degradation	Non-ionizing dose (NIEL) and equivalent fluence	Proton beams (~ low energy)
Single-event upset or latch-up for example	LET spectra (ions) Proton energy spectra, explicit SEU/L rate	Heavy ion particle beams Proton particle beams ←
Sensor interference (background signals)	Flux above energy threshold, flux threshold Explicit background rate	Radioactive sources, particle beams
Internal electrostatic charging	Electron flux and fluence Dielectric E-field.	Electron beams Discharge characterization

 \Leftarrow = test data feedback to calculation

e, p =electron, protons



G.2 Future models

There are several efforts underway relating to radiation belt, solar particle and cosmic ray environment and interaction models which will probably lead to future internationally-acceptable standards.

Many of these models are available in the Space Environment Information System (Spenvis) at http://www.spenvis.oma.be/spenvis/.

TREND project (ESA-funded):

- BIRA/IASB development of empirical models of the low altitude environment derived from AZUR, SAMPEX and UARS, especially relating to energetic protons and their directionality. The measurements from MIR reported by PSI are also of interest in this context [RDG.1].
- MSSL (UK), development of models based on the Meteosat (geostationary) environment monitor and, together with A. Vampola, a CRRES-based model.
- MPAe (D) and MSSL (UK), development of a medium-energy electron model at high altitudes based on ISEE data.

CERT/DERTS

A French-funded consortium are developing techniques for deriving transient radiation belt morphologies and empirical models from physical principals via computer simulations of magnetospheric disturbances and injection events.

US efforts

CRRES-related efforts:

- Phillips Lab. Geophysics Directorate are developing a series of engineering radiation-belt models based on the CRRES mission; a proton model (CRRES-PRO), an electron model (CRRESELE), and a total dose model (CRRESRAD) have been released.
- A. Vampola: using CRRES data, development of MEA model and an outerzone model based on a neural network analysis of CRRES data, its link with geomagnetic indices, and the historic record of these indices.
- CHIME is a cosmic ray environment model developed by the USAF Phillips Laboratory on the basis of CRRES measurements.

Other US efforts

- Boeing are developing models of the low altitude environment based on NOAA particle environment monitor data. Solar cycle variations and links with atmospheric density variations are being modelled.
- Naval Research Laboratories have developed but not generally released, an update of the CREME model, CREME96, including an improved model of the solar cycle modulation, improved physical and geomagnetic shielding models, and a worst-case solar particle event based on the October 1989 event. This effort was a collaboration with Moscow State University. A WWW-site has been established (http://crsp3.nrl.navy.mil/creme96/).

Russian efforts

Moscow State University are developing:

- A low altitude electron environment model;
- A cosmic ray model (in collaboration with NRL);
- Solar particle environment models;
- Models of heliospheric modulation of cosmic and solar energetic particles.

COSPAR task group

With IASB as convenor (D. Heynderickx, Belgisch Instituut voor Ruimte-Aeronomie, Ringlaan 3, B-1180 Brussel; http://www.magnet.oma.be/), a special task group has been established by COSPAR with a view to coordinating the various radiation belt modelling efforts in order to eventually produce international consensus standard radiation belt models.



ISO standard efforts

ISO TC10/SC14/WG4 on space environment models are overseeing the development of various environment models, with Russia as convenor. It is intended that this ECSS Standard stays harmonized with ISO standards but new models are not expected in the near future.

G.3 Sources of models

AE-8, AP-8 NSSDC, NASA-Goddard Space Flight Center. Models can be downloaded from the FTP address:
 nssdc.gsfc.nasa.gov/pub/models/radbelt. Models can be accessed via www: http://nssdc.gsfc.nasa.gov/space/model/, and are available in Europe via D. Heynderickx,
 Belgisch Instituut voor Ruimte-Aeronomie, Ringlaan 3,
 B-1180, Brussel; (http://www.magnet.oma.be/ as part of UNIRAD and Spenvis.

SHIELDOSE Stephen M. Seltzer, Ionizing Radiation Division, National Institute of Standards and Technology, Gaithersburg MD 20899, USA; seltzer@enh.nist.gov; also available through NEA library, CCC-379 and available in Europe via D. Heynderickx, Belgisch Institute voor Ruimte-Aeronomie, Ringlaan 3, B-1180, Brussel; http://www.magnet.oma.be/as part of UNIRAD and Spenvis.

CREME National Geophysical Data Center, Code E/GC2, Dept. 946 325 Broadway Boulder Co 80303 3328 USA (Although developed by NRL, NOAA act as distribution agents).

CREME-96 Naval Research Laboratory Department of the Navy Code 7654 Washington, DC 20375 USA http://crsp3.nrl.navy.mil/creme96/

JPL-1991 J. Feynman, JPL, 4800 Oak Drive, Pasadena, Ca 91109, USA.

CRRESELE, USAF Phillips Lab, Geophysics Directorate PL/GPS, CRRESPRO, Hanscom AFB Ma.01731 USA
CRRESRAD

EQFRUX, B. E. Anspaugh, JPL, 4800 Oak Drive, Pasadena, Ca **EQGAFLUX** 91109, USA

G.4 Internal electrostatic charging analysis tools

Internal electrostatic charging (or deep-dielectric charging) results from the build-up over a period of up to several days of electrostatic charge. For hazardous levels to be reached, the environment normally shall be characterized by high levels of energetic electron flux. The charge build-up depends on:

- the severity of the environment and its duration;
- the dielectric resistivity of the susceptible part (or lack of grounding of floating metalization);
- effects such as radiation induced conductivity.

While discharge can also depend on properties such as geometry and material condition. Charge build-up can therefore be mitigated by choice of material and grounding, but also by employing shielding to reduce the severity of the environment.

Tools are available to address these issues, such as ESADDC [RDG.2] which employs a Monte-Carlo radiation transport method to compute the charge buildup



in a dielectric material behind specified shielding in a certain input environment. Efforts in tool development seek to simplify this approach into a robust engineering tool. ESA's effort, by means of sponsoring a collaboration between DERA(UK) and DERTS(F), removing especially the need for Monte-Carlo analysis and introducing a method to specify the hazard, has resulted in computational tools which have been incorporated in the Space Environment Information System http://www.spenvis.oma.be/spenvis/.

G.5 Further information

Further information on analysis of space radiation environments and effects can be found on various WWW sites:

ESTEC Space Systems http://www.estec.esa.nl/wmwww/wma

Environment Analysis Site

ESA/IASB Space Environment http://www.spenvis.oma.be/spenvis/

Information System

NASA Space Environment and http://see.msfc.nasa.gov/

Effects Site

G.6 References

- RDG.1 Bühler P., L. Desorgher, A. Zender and E. Daly, "Observation of the Radiation Belts with REM", Proceeding of the ESA Workshop on Space Weather, ESA-WPP-155 (1998).
- RDG.2 Sorensen, J., "An Engineering Specification of the Internal Charging" Proceeding of the Symposium on Environment Modelling for Space-Based Applications, ESA-SP-392, December 1996.



Annex H (informative)

Particulates

H.1 Space debris flux models

H.1.1 General

Two developed space debris population models are the Meteoroid And Space Debris Terrestrial Environment Reference Model (MASTER-97) [RDH.1] and a NASA engineering model, ORDEM-96 [RDH.2]. These models can be used as interim solution for impact risk assessments and shielding design purposes until a specific standard for the space debris environment is defined.

H.1.2 MASTER-97

MASTER-97 uses a semi-deterministic approach which represents the debris environment by modelling its history from the beginning of spaceflight to present. It uses three source terms for the debris population: launches, explosions and collisions and follows their orbital evolutions. The space debris population at an epoch of 31 March 1996 is derived from 132 low and high intensity on-orbit break-ups.

A linear growth rate of 2 percent (uniform for all sizes) is applied for other years. Solar cycle effects on cleansing rate are included as for the NASA engineering model given in [RDH.3].

Mass (or diameter) dependent binning is used to assign weights to a condensed population of about 240 000 objects larger than 0,1 mm.

An Analyst application allows to interrogate the spatial debris distribution to determine collision fluxes for an arbitrary target orbit passing through the control volume. Flux results can be analysed with respect to collision velocity magnitude, its direction (azimuth and elevation), the orbit location, and the 3D position where the flux was encountered.

MASTER is provided on a CD-ROM containing the stored, binned data together with some processing software.

A simplified version, called the MASTER engineering model, is available as well. This version is applicable for target orbits with small eccentricities.

H.1.3 ORDEM-96

The NASA engineering model, ORDEM-96, analytically represents similar sources to MASTER plus additional non-fragmentation source distributions like



paint flakes, Aluminium Oxide particles from solid rocket motor burns and Sodium/Potassium droplets. These non-fragmentation sources mainly contribute to the small size population. The model is also derived from recent radar measurements and impact data from retrieved surfaces. The debris environment distribution is approximated with six different inclination bands. Each band has a unique distribution of semi-major axis, for circular orbits, and a unique perigee distribution for highly elliptical orbits. In addition, each inclination band has a unique, analytically defined size distribution which depend on the source of debris.

Collision probability equations are used to relate the orbital element distributions of the population to the flux measured on a spacecraft or to the flux measured through the field of view of a ground sensor. It provides directional information of the impacting flux. The model is computer based.

H.1.4 Velocity distribution

Impact velocities can range from 0 to about 15,5 km/s with an average velocity of 10 km/s for low inclination and of 12 km/s for high inclination orbits.

H.1.5 Mass density

According to [RDH.3], the average density of particles larger than 0,62 cm in diameter is assumed to be:

$$\rho = 2.8d^{-0.74} \text{ g/cm}^3$$
.

The average density of smaller space debris particles is thought to be in the range $2.8 - 4.7 \text{ g/cm}^3$. The values to be used for design are given in H.1.6.

H.1.6 Regime of applicability

The MASTER-97 space debris model [RDH.1] is applicable for particle sizes larger than 0,1 mm and for circular and elliptical Earth orbits up to geostationary altitudes.

The ORDEM-96 space debris model [RDH.2] is applicable for particle sizes larger than 1 micron and for circular and elliptical Earth orbits up to altitudes of $2\,000~\mathrm{km}$.

H.1.7 Tailoring guidelines

Nominal and worst case debris model parameters and mass densities are:

Table H-1: Nominal and worst case debris model parameters and mass densities

Parameter	Nominal	Worst case
solar activity, S	140	70
ref. mission year, t	middle	last
debris density ρ [g/cm ³]	4,0	8,0

For design purposes the nominal parameter values shall be used. A spherical shape shall be assumed to convert particle masses and diameters. Values for the solar activity, S, at specific times within a solar cycle can be found in clause 6. The default growth rates for the respective models shall be used. For the assessment of impact effects the full velocity distribution of space debris should be used. For a preliminary analysis a constant debris impact velocity of 10 km/s shall be used. Uncertainty factors for space debris fluxes (see H.2) shall not be applied.

H.1.8 Other debris models

Several other space debris models are in use or under development. These models can be used in special cases for impact analyses or risk assessments if the user



is familiar with the features and range of validity of the models. Two of these models are mentioned below.

H.1.8.1 NASA-90 model

From about 1990 until 1996 the NASA space debris engineering model defined in [RDH.3] has been most widely used for design applications. This model is given in terms of simple analytical expressions. It is relatively easy to use and widely distributed. However, it has some known shortcomings of which the assumption of spherical orbits for all debris particles is probably the most severe. The model can still be used for some initial risk assessments, however, the user should be aware of its shortcomings.

H.1.8.2 IDES

The Integrated Debris Evolution Suite (IDES) [RDH.4] space debris model uses a deterministic representation of individual objects > 10 cm and a statistical representation of the populations between 10 μ m and 10 cm (by fragment orbit discretization in dimensions of perigee, radius, eccentricity, inclination and mass).

Considered debris source terms include launch related objects, high and low intensity explosions, collisions, paint flaking and secondary ejecta. These sources are modelled and evolved from the beginning of the space age to the present day and into the long term future. For impact risk assessments the directional and velocity distribution of the encountered flux is included. Circular and elliptical target orbits can be analysed. IDES is applicable to LEO altitudes and for particle sizes larger than 10 μ m. The tool also allows to study the long term evolution of the debris population and the long term impact risk to target orbits under different traffic scenarios, and the effectiveness of different mitigation measures.

H.2 Model uncertainties

H.2.1 General

The meteoroid and space debris environment flux models given above contain several known approximations and other uncertainties.

H.2.2 Meteoroids

According to [RDH.3] uncertainties in the meteoroid models mainly result from uncertainties in particle densities and masses. Fluxes for meteoroids larger than 10^{-6} g are well defined, but the associated masses are quite uncertain. The mass density of meteoroids spans a wide range, from about 0,15 g/cm3 to values as large as 8 g/cm³. At a set mass this implies an uncertainty in the flux of a factor 0,1 to 10. For meteoroids smaller than 10^{-6} g flux uncertainties at a given mass are estimated to be a factor of 0,33 to 3.

H.2.3 Space debris

The space debris flux models were developed as a best estimate rather than a conservative one. In [RDH.3] uncertainties for debris fluxes in different size regimes are quoted. These factors give the 90 % confidence level that the real debris flux is within a bandwidth defined by the model flux multiplied by the uncertainty factors.



Table H-2: Uncertainty of 90 % confidence level for debris flux

Particle size	Uncertainty factor
d > 10 cm	0,5 to 1,5
0,05 cm < d < 10 cm	0,33 to 3,0
d < 0,05 cm	0,5 to 2,0

Other uncertainties of the debris model include

- the debris density,
- the debris shape,
- the annual growth rates,
- the altitude dependence, especially for altitudes above 800 km,
- the velocity distribution, especially for low impact velocities, and
- the dependence on solar activity.

A more detailed discussion of model uncertainties is given in [RDH.3 and RDH.2].

H.3 Damage assessment

In this clause a brief general overview of damage assessment criteria and procedures is given.

For each individual project the damage assessment shall be tailored according to the specific conditions and requirements (e.g. orbit, shielding, damage criteria, required reliability).

Any damage assessment depends to a large extend on the relevant failure criteria. Possible failure criteria include:

- cratering (sensor degradation, window blinding, surface erosion);
- larger craters (sealing problems, short circuits on solar arrays);
- impact generated plasma (interference, discharge triggering);
- impulse transfer (attitude problems);
- spallation from inner wall (equipment damage, crew injury);
- wall penetration (damage, injury, loss of liquid or air);
- burst, rupture (pressurized parts);
- structural damage.

For a quantitative damage and risk assessment so called damage or design equations for the given shielding configuration are needed. They give shielding thresholds or hole sizes for given impacting particle parameters and failure mode.

One of the most widely used damage equation gives the threshold thickness for penetration of single metal plates (thin plate formula):

$$t = k_m m^{0.352} \rho^{0.167} v^{0.875}$$

where

t is the threshold thickness for penetration;

 k_m is the material constant, 0,55 for Aluminium;

m is the mass of projectile (g);

 ρ is the density of projectile (g/cm³);

v is the normal impact velocity component of projectile (km/s).



A puncture occurs whenever the threshold thickness for an impacting particle with given mass, density and velocity exceeds the shielding thickness of the surface under consideration.

Finding a realistic damage equation for a given shielding configuration can be problematic.

The translation of a failure mode to a damage equation can be difficult. Many damage equations for different types of shields and for different velocity regimes have been developed. However, for most materials, compounds, and shielding concepts no specific damage equation is available.

Sometimes scaled effective thicknesses in combination with known damage equations can be used for a first assessment.

For impact damage and risk assessments secondary ejecta should be considered as well. Every hypervelocity impact leads to the ejection of secondary particles which can impact other surfaces (depending on the spacecraft geometry). The total mass of the ejected particles can exceed the mass of the primary impactor by orders of magnitude. Secondary particles will be typically ejected within a cone around the impact direction. Their velocities are typically below 2 km/s.

At present, quantitative models of secondary ejecta are not mature enough to be used as standard.

H.4 Analysis tools

H.4.1 General

Several numerical tools have been developed to perform impact and impact risk analyses. The following tools are mentioned for information only. Other tools can be used as well if they are based on the reference flux models.

H.4.2 Deterministic analysis

For information and analysis of the deterministic, trackable space objects, the DISCOS database was developed [RDH.5]. DISCOS (ESA's Database and Information System Characterising Objects in Space) is a catalogue on Earth orbiting space objects and debris.

DISCOS can be used to extract detailed data on all the tracked objects and it also provides facilities to manipulate those data (forward propagation, data presentation). DISCOS is implemented at and maintained by ESA/ESOC. It is accessible for registered users only.

H.4.3 Statistical analysis

A statistical tool, ESABASE/DEBRIS, was developed for a detailed impact risk assessment of smaller, non-trackable particles [RDH.6]. ESABASE/DEBRIS is a fully three dimensional numerical analysis tool including directional and geometrical effects and spacecraft shielding considerations. It is based on environment and particle/wall interaction models and includes the reference meteoroid and space debris flux models defined in this document.

The user specifies the mission, spacecraft geometry, attitude and shielding as well as the particle type, size and velocity range to be analysed. The computed output includes:

- the number of impacts;
- the resulting number of damaging impacts taking into account the spacecraft shielding and damage assessment equations;
- the mean particle impact velocity (amplitude and direction);
- the numbers of craters of specified size;
- the probability of no failure.



ESABASE/DEBRIS allows the optional use of several meteoroid and debris flux models.

H.5 Lunar dust simulant

Various simulants have been prepared in the laboratory to mimic the properties of lunar dust. One well-known simulate is the Minnesota Lunar dust simulate that can be obtained from:

Space Science Centre, University of Minnesota, Minneapolis.

This simulate reproduces the chemical composition of lunar dust as well as its microscopic morphology. It does not reproduce well the mechanical properties of in situ lunar dust, due to the absence of Van der Waals forces between grains at ambient pressure.

H.6 References

- RDH.1 Klinkrad H., J. Bendisch, H. Sdunnus, P. Wegener, R. Westerkamp, "An Introduction to the 1997 ESA MASTER Model", Proc. of the Second European Conf. on Space Debris, pp. 217-224, ESA SP-393, May 1997.
- RDH.2 Kessler D.J., J. Zhang, M.J. Matney, P. Eichler, R.C. Reynolds, P.D. Anz-Meador and E.G. Stansbery, "A Computer Based Orbital Debris Environment Model for Spacecraft Design and Observations in Low Earth Orbit"; NASA TM 104825, November 1996.
- RDH.3 Anderson B.J., "Natural Orbital Environment Guidelines for Use in Aerospace Vehicle Development", by:, editor and R.E. Smith, compiler; NASA TM 4527, chapter 7, June 1994.
- RDH.4 Walker R., S. Hauptmann, R. Crowther, H. Stokes and A. Cant, "Introducing IDES: Characterising the Orbital Debris Environment in the Past, Present and Future", Paper AAS 96-113, Advances in the Astronautical Sciences, Vol. 93 Part I, 201-220, 1996.
- RDH.5 Klinkrad H., U. Fuller, J.C. Zarnecki, "Retrieval of Space Debris Information from ESA's DISCOS Cataloque", Proc. ESA Workshop on Space Environment Analysis, Noordwijk, 9-12 October 1990.
- RDH.6 Drolshagen G. and J. Borde, "ESABASE/DEBRIS, Meteoroid/Debris Impact Analysis, Technical Description", ref. ESABASE-GD-01/1, 1992.



Annex I (informative)

Contamination

I.1 Existing Tools

The computer codes dedicated to spacecraft contamination are presented here in clauses I.2 to I.11 from information available in literature. All of them are simulation tools at system level, except the CONTAM III code, clause I.4, that is devoted to thruster plume modelling. The clause I.12 presents identified data bases, although some of the simulation codes also contain integrated (limited) data bases. When available, the integration in a global tool that allows to automatically take into account parameters, such as surface temperatures (from thermal models), mission description and atmospheric models, is also mentioned.

The main field of applicability of the codes is external contamination either in LEO or GEO. However, some of the programs, as described in each section, have limited transport modelling capabilities (simple or improved view factors only), and gives poor results in cases when return-flux through ambient-scatter and self-scatter is important, i.e. essentially in "lowest LEO" (at altitudes below 500 km-700 km or even more at lower altitudes typical of Shuttle, MIR or ISS). At such altitudes, pressure increase due to ram flux can go as high as $10^{-5}~\mathrm{hPa}$ – $10^{-4}~\mathrm{hPa}$, resulting in decametric to metric mean free path, which makes collisions really not negligible and collisional return-flux important (typically of the order of the percent).

The capability to model semi-enclosed systems is not often reported in literature. However, provided these can be modelled, which seems to be possible for most of the codes, semi-enclosed systems can be modelled as well. Here again, some codes can be limited due to too poor transport modelling in case of high pressures. A difference with external contamination computing for which collisional return flux may often be the main contamination process (for surfaces not in direct view), is that in closed systems direct surface to surface collisionless transport (with possible surface reflections) is most of the time the dominant process. Except for high pressures such as 10^{-3} hPa (and thus decimetric mean free path), which can be found in semi enclosed systems yet.

I.2 ESABASE: OUTGASSING, PLUME-PLUMFLOW and CONTAMINE modules

ESABASE is a general spacecraft modelling tool including several modules developed by several parties under ESA sponsorship, and now supported by GEC ALSTHOM, UK.



In its currently available version, ESABASE essentially deals with contamination through its OUTGASSING module, developed by Matra Marconi Space (MMS). It allows to compute contaminant deposit on spacecraft by numerical integration:

- sources: material outgassing by standard laws (see 11.5.1.1), the surface temperatures being obtained by the thermal analysis module;
- transport: by mass-transport factors computed from view factors (collisionless transport) improved by adding the possibility of one collision per particle trajectory with background densities (i.e. fixed, not self-consistent) of ambient and outgassed species, as described in 11.5.2.1.2;
- deposition on surfaces: deposited mass computed, reemission or immediate reflection allowed.

The PLUME module currently implemented in ESABASE simulates thruster plume expansion. It was derived from CONTAM code and does not correctly model plume backflow (see the section about CONTAM for details). It is thus essentially used for forces and torques, and thermal analysis.

As a conclusion, the current version of ESABASE is consequently rather limited in two major aspects of contamination:

- contamination by thruster backflow (and droplets);
- more collisional transport mechanisms in case of particularly sensitive surfaces (e.g. cooled optics) that are baffled and can only be reached after some collisions, or even one collision, which is crudely modelled by OUTGASSING through very approximate background densities (not modified by spacecraft for ambient density, and with spherical symmetry for outgassed density [RDI.1]).

Yet, several improvements or new modules have been developed recently by MMS [RDI.2] under CNES sponsorship, and the new improved version is available in ESABASE.

First, the PLUME module has been improved:

- Its PLUMFLOW sub-module, modelling the dynamics of the thruster itself, has been added a two-dimensional multi-species DSMC model of nozzle lip region, in order to describe thruster backflow correctly now.
- Droplets produced by bi-propellant thrusters have been included. Their distribution is taken from experiments, and their trajectories are followed in straight lines until possible surface impingement.

Secondly, a new module called CONTAMINE has been added. It computes surface interactions (adsorption, diffuse reflection, specular reflection) and above all surface effects: modification of thermo-optical, electrical and mechanical properties, or global output power reduction for solar cells. These property changes are either taken from data gathered in a data base included in CONTAMINE (with interpolation between available data, which are not always very numerous), or complex index computed. It can also be interfaced with the older OUTGASSING module to compute deposit thickness including re-emission.

This new contamination capability of ESABASE should now allow a good prediction of thruster contamination. It remains to be validated by comparison with experiments (see TRICONTAM experimental validation, which can be partially considered as validating ESABASE modules). The limited capability of the quasicollisionless transport model, that was pointed out above, remains in this new version.

I.3 JMC3D

JMC3D is a tri-dimensional Monte-Carlo code developed by Aérospatiale, Les Mureaux, France. It seems to have been initially devoted to Hermes re-entry phase modelling, but has also been applied to Ariane 5 and spacecraft contamination simulation [RDI.3]. It exhibits the following features:



- molecular rotational degrees of freedom taken into account;
- specular/diffusive surface reflections, with possible accommodation;
- inclusion of thruster flow computed by Euler method (application to Shuttle);
- variable time step and weighting factors;
- un-structured objects and volume mesh;
- vectorized code (on CRAY computers).

The few data available indicate acceptable agreement with experiments: good accuracy for Hermes high densities and the order of magnitude for Shuttle backflow.

It seems to be a rather high-standard model (molecular rotational degrees of freedom, un-structured mesh), although the small number of publications about it makes it difficult to know whether it includes the necessary "technical" features to be used for satellites (versatile geometry and thruster flow modelling, contaminant effects). JMC3D is an Aérospatiale developed model presently not diffused to other companies.

I.4 CONTAM 3.2 or CONTAM III

CONTAM has been developed from the late seventies to the mid eighties by Science Application International Corporation (SAIC) for the Air Force Rocket Propulsion Laboratory (AFRPL). It is one of the most well known and widely used computer code for computing the plume flowfields of monopropellant, bipropellant or solid rocket thrusters. Spacecraft contamination assessment thus requires this model to be included as a contaminant source in a contaminant transport/effects model, as it has been done in ESABASE (PLUMFLOW module developed by MMS but based on CONTAM) or in the TUHH contamination model TRICONTAM [RDI.4].

The computational methods and physics included are described in many references [RDI.5]. It computes both steady state and transient combustion processes. Computed gaseous outflow includes unburned propellant, unburned droplet or solid particles, and liquid wall film. The two-phase fluid dynamics is treated by the method of characteristics, possibly including one shock or none (depending on the thruster). Non-equilibrium chemical kinetics is computed along streamlines in a one-dimensional model. The droplets (liquid engine) or solid particles (solid engine) dynamics is computed in the flowfield, including condensation/evaporation.

In such inviscid flow field computations, the boundary layers (along nozzle walls) shall be treated separately, as it is the case in CONTAM. Boundary layers are of prime importance for contamination because they determine the transition region around the nozzle lip and thus the backflow. Only thin turbulent boundary layers of large propellants were included in the first version of the code. Improvements have been implemented on the next version (CONTAM 3.2), including thicker viscous laminar boundary layers of smaller thrusters and the possibility for the user to define some parameters "by hand". However, the modelling of the transition region around nozzle lip remains a simple Prandtl-Meyer expansion from the boundary layer at the lip. The backflow rate remains consequently approximate, and diffusion and species demixing at lip are not included. This makes the simple use of CONTAM for backflow contamination rather inaccurate. This is the reason why several people supplemented CONTAM with a DSMC model of nozzle lip flow (in the PLUMFLOW module to be included by MMS in ESABASE, and for a specific case in [RDI.6]).

Droplets are emitted at smaller angles, and the modelling of their dynamics seems more accurate. The reader can also look at the experimental validation of the TRICONTAM code derived from CONTAM in the section below.



I.5 TRICONTAM

TRICONTAM, a global contamination model developed at Technical University Hamburg Harburg (TUHH), Germany, has been developed under ESA/ESTEC contract. It seems to be essentially devoted to computing contamination from thruster plume exhausts. The plume flowfield is computed by an improved version of CONTAM III (essentially concerning transient combustion processes and chemistry), and the contaminant transport to spacecraft surfaces is assumed to be collisionless. An important part of the software is dedicated to forces, torques and thermal analysis.

The major interest of that code is that its results were compared to the numerous experimental measurements realized at TUHH [RDI.4]. As the plume model of TRICONTAM was improved with respect to CONTAM III, this very valuable experimental validation of the code can unfortunately not be considered as a full validation of CONTAM III (or other evolutions of CONTAM III, such as the one to be implemented in ESABASE/PLUMFLOW). The validation results can be sketched here (from [RDI.4]):

- Plume gas composition (module specific to TRICONTAM): good, to be supplemented with some rare species like HCN and NO.
- Gas streamlines up to 90° divergence (similar to CONTAM and certainly ESABASE/ PLUMFLOW): good.
- Gas backflow, divergence angle greater than 90° (similar to CONTAM III worse than ESABASE/PLUMFLOW which includes a DSMC model of nozzle lip): total flow not very good, and no mechanism included to account for species demixing.
- Droplets (module specific to TRICONTAM, modified from CONTAM III): good concerning droplet dynamics, even for pulsed firings, but not very good concerning droplet size and composition; possibility of droplet outflow from wall film towards backflow not modelled.

I.6 SOCRATES

The SOCRATES code (Spacecraft/Orbiter Contamination Representation Accounting for Transiently Emitted Species) was developed by Spectral Sciences for the Phillips Lab., Hanscom Air Force Base, Massachusetts.

It is one of the most elaborate contamination tools concerning collisional transport and gas-phase reactions [RDI.7]. It is a true DSMC (Direct Simulation Monte Carlo), which thus simulates realistically collisions, including reactions: any kind of bi-molecular collision, excitation, reaction, dissociation into several products, photon production. Molecular internal energy (vibrational) is taken into account (Borgnakke & Larsen model). A special treatment of highly collisional regions, where thermal equilibrium is reached, is implemented.

Two nested meshes, an inner and an outer one, are included one in the other, which allows to compute both short and long distance effects.

The contaminant sources are much simpler: standard outgassing sources and thrusters described by the analytical formula:

$$\phi(r, heta) \propto rac{e^{-C(1-\cos(heta))}}{r^2}$$

where

r is the distance to thruster exit;

 θ is the angle with respect to thruster axis;

 ϕ is the thruster efflux density at position r, θ ;

C is a constant.



Output quantities also aim at gas phase physics: return fluxes can be obtained, but much more gas phase data can be computed, such as species (relative) velocities, temperatures and collision or reaction rates.

I.7 SPACE II

The Shuttle or Payload Contamination Evaluation code (SPACE) was developed since the late seventies by Martin Marietta to predict the contamination of the Shuttle and Spacelab [RDI.8]. Only a reduced number of possible geometries have thus been included: Spacelab, the Shuttle with various possible payloads (IECM...).

Contaminant sources are:

- surfaces: early desorption, outgassing and also evaporation.
- specific parametric description of vents, leakages, Shuttle flash evaporators and thrusters (Simons' model [RDI.9] but with the possibility to include CONTAM plumflow model).

The transport model is of an hybrid type. First order transport is done by view factor computing. Surface reflections are also included. Second order transport through gas phase collisions is added following Bhatnager-Gross-Krook simplified method: it is in fact a Monte-Carlo ray-tracing technique (importantly) improved by considering "secondary emitters" accounting for collisions in the volume surrounding the Shuttle, with rates and distribution functions computed by BGK method [RDI.10]. A next improvement allows to also take into account third order effects: the attenuation of fluxes between these volumic "secondary emitters" and the impinged surfaces [RDI.10]. Column-density can be computed. Standard surface output is deposition thickness, but no contamination degradation effects routines are included.

I.8 MOLFLUX

MOLFLUX (MOLecular FLUX) was developed for NASA by Martin Marietta Aerospace and Lockheed Engineering & Sciences Company. It has been used for a long time in industry. It seems moreover to have been chosen by NASA as the model to be used by all American ISS participants to predict contamination [RDI.11].

Contaminant transport is computed at first order by view factors that shall be computed separately by thermal radiation program TRASYS. Similarly to SPACE II model, second order collisional transport is computed by an approximate BGK method [RDI.2], which certainly makes both models very close.

Global sticking coefficients S for contaminants coming form surface i to surface j are taken equal to [RDI.12]

$$S = \begin{cases} T_{i} - T_{i} & 0 & \text{for} & T_{i} > T_{j} \\ \frac{T_{j} - T_{i}}{200} & \text{for} & T_{i} < T_{j} & \text{and} & T_{i} > T_{j} - 200 \\ 1 & \text{for} & T_{i} < T_{j} - 200 \end{cases}$$

which seems to have been chosen more generally for ISS contamination modelling.

Program outputs are column densities and contaminant deposit thickness.



I.9 ISEM

The Integrated Spacecraft Environments Model (ISEM) is presented as the next generation of contamination models developed for NASA, following SPACE and MOLFLUX [RDI.13]. It has been delivered to NASA Goddard and Marshall Space Flight Center, but also JPL, Fairchild, Boeing and the Applied Physics Laboratory (APL).

The transport modelling technique seems to be the same as in SPACE and MOL-FLUX, with some improvements [RDI.13]. It has the advantage to be quicker than DSMC but lacks of accuracy in case of high densities or multi-collisional transport.

The improvements with respect to SPACE or MOLFLUX are essentially in the possibility of modelling new phenomena:

- multiple surface reflections;
- atomic oxygen erosion as contaminant source;
- ion production by UV or charge exchange;
- UV emission from excited emitted N2.

or doing things more conveniently:

- putting imaginary surfaces in the volume without re-running geometry model;
- modelling the inside of a vacuum chamber included;
- possibility to operate in atmospheres of Venus and Mars.

1.10 OPT

The Orbital Particulates Trajectory model (OPT) was developed by Applied Science Technologies, partially on NASA funding, partially on own funding [RD I.13]. It computes particulate transport on spacecraft.

Particulate sources shall be defined by the user, with a possibility to generate them at random with a specified distribution.

Particulate transport takes into account:

- gravitational effects (non-sphericity of the earth, lunar-solar effects);
- atmospheric drag;
- solar radiation pressure;

but nothing due to the presence of spacecraft itself (e.g. pressure increase and electrostatic effects), and OPT can be seen as a simple orbitography code applied to particulates.

I.11 CAP

Contamination Analysis Tool (CAP) developed by JPL for NASA (Goddard) is a basic tool, including standard first-order emission rate, collisionless transport with surface diffuse reflections and accommodation [RDI.14]. An example of application of CAP is described in [RDI.15].

1.12 Databases

Some of the tools described above include databases about contamination effects. References to two other important databases created independently of any model were found in literature. They can be used to assess contamination effects from contaminant deposit and column densities computed by these models.

A first database was created by Boeing Aerospace & Electronics in 1986-1988 for Air Force Wright Research and Development Center [RDI.16]. Its availability to non-Americans is not reported. It is a very important work resulting from the collection of over 3000 sources and covering most of contamination fields.



The Plume Contamination Database (PCD) was developed by MMS for ESTEC, using ORACLE [RDI.2]. It is anticipated that the database is progressively filled by ESTEC contractors and presently essentially contains measurements made at TUHH [RD I.17].

I.13 References

- RDI.1 Koeck C., Frezet M., Calculation of environmental effects on space-craft surface using Monte-Carlo technique application to contamination and atomic oxygen, Proceedings of the Fourth International Symposium on Materials in a Space Environment, Toulouse, France, Sept. 6-9, 1988, pp 263-273.
- RDI.2 Chéoux-Damas P., Théroude C., Castejon S., Hufenbach B., PCD: An interactive tool for archiving plume impingement and contamination data, to be published in The Proceedings of the Second European Spacecraft Propulsion Conference, ESTEC, Noordwijk, The Netherlands, May 27-29, 1997, p. 587-594.
- RDI.3 Delamare B., Dumas L., 3D Monte-Carlo simulation of contamination induced by shuttle RCS engines, Proceedings of the Sixth International Symposium on Materials in a Space Environment, Noordwijk, The Netherlands, Sept. 19-23, 1994, pp 39-44.
- RDI.4 Trinks H., Exhaust Plume Data Handbook (EPDH IV), Progress Report IV, ESA Contract No 7510/87/NL/PP, Sept. 1991a.
- RDI.5 Hoffman R. J., Kawasaki A., Trinks H., Bindemann I., Ewering W., The CONTAM 3.2 plume flowfield analysis and contamination prediction computer program: Analysis model and experimental verification, AIAA paper No 85-0928, AIAA 20th Thermophysics Conference, Williamsburg, VA, June 19-21 1985.
- RDI.6 Guernsey C. S., McGregor R. D., Bipropellant rocket exhaust plume analysis on the Galileo spacecraft, AIAA paper No 86-1488, AIAA/ASME/SAE/ASEE 22nd Joint Propulsion Conference, Huntsville, AL, June 16-18, 1986.
- RDI.7 Elgin J., Bernstein L. S., The theory behind the SOCRATES code, NASA STAR 93N24298, AD-A259987, Final Report, Aug. 1992.
- RDI.8 Jarossy F. J., Pizzicaroli L. C., Owen N. L., Shuttle/payload contamination evaluation (SPACE) program improvements, Shuttle optical environment; Proceedings of the Meeting, Washington, DC, April 23-24, 1981, pp 78-85.
- RDI.9 Simons G.A.: "Effect of Nozzle Boundary Layers on Rocket Exhaust Plumes", AIAA Journal, Tech. Notes, vol.10, Nø 11, 1972, pp. 1534-1535.
- RDI.10 Ehlers H. K. F., An analysis of return flux from the space shuttle orbiter RCS engines, AIAA paper No 84-0551, AIAA 22nd Aerospace Sciences Meeting, Reno NV, Jan. 9-12, 1984.
- RDI.11 Babel H, Hasegawa M., Jones C., Fussell J., The effects of contamination from silicones and a modified-Tefzel insulation, IAF Paper 96-I.5.08, 47th International Astronautical Congress, Beijing, China, Oct. 7-11, 1996.
- RDI.12 Cognion, R., MOLFLUX analysis of the SSF electrical power system contamination, AIAA paper 91-1328, AIAA 26th Thermophysics Conference, Honolulu, HI, June 24-26, 1991.
- RDI.13 Rantanen R., Gordon T., On-orbit transport of molecular and particulate contaminants, Optical system contamination V and stray light and system optimization; Proceedings of the Conference, Denver, CO, Aug. 5-7, 1996, (SPIE Proceedings. Vol. 2864), 1996, pp. 115-126.
- RDI.14 Millard J. M., Jet Propulsion Laboratory Contamination Analysis Program - Programmer and User Manual (with appendix), JPL report No 715–55, Prepared by the Jet Propulsion Laboratory for the Goddard Space Flight Center, 1980.



- RDI.15 Barengoltz J. B., Millard J. M., Jenkins T., Taylor D. M., Modeling of internal contaminant deposition on a cold instrument sensor, Optical system contamination: Effects, measurement, control II; Proceedings of the Meeting, San Diego, CA, July 10-12, 1990, pp 337-351.
- RDI.16 Thorton & Gilbert: "Spacecraft contamination database", SPIE Volume 13, 29; Optical System Contamination: Effects, Measurement and Control-2; 1990. pp 305-319.
- RDI.17 Trinks H., Surface Effet Data Handbook (SEDH III), Progress Report V, ESA Contract No 7510/87/NL/PH, Sept. 1991b.



ECSS	CSS Document Improvement Proposal		
1. Docume	ent I.D.	2. Document date	3. Document title
ECSS-E-10	0-04A	21 January 2000	Space environment
4. Recomm		ent (identify clauses, subclauses	
	for recommenda		
_	tor of recommen		
Name:		Organization:	
Address:		Phone: Fax: e-mail:	7. Date of submission:
8. Send to	o ECSS Secretaria	at	
Name: W. Kriedte ESA-TOS/0		Address: ESTEC, P.O. Box 299 2200 AG Noordwijk The Netherlands	Phone: +31-71-565-3952 Fax: +31-71-565-6839 e-mail: wkriedte@estec.esa.nl

Note: The originator of the submission should complete items 4, 5, 6 and 7.

This form is available as a Word and Wordperfect–Template on internet under $http:/\!/www.estec.esa.nl/ecss/improve/$



(This page is intentionally left blank)